# A Search for Single Top-Quark Production and Flavour-Changing Neutral-Current Interactions at H1


Thesis submitted in accordance with the requirements

of the University of Liverpool

for the degree of Doctor in Philosophy

by

John James Kennedy

September 2002

**Abstract**

A search for anomalous single top-quark production mediated by a flavour-changing neutral-current coupling, $\gamma - u - t$ is performed exploiting data collected in $e^+p$ collisions at HERA between 1994 and 2000. The search is motivated by the previous observation of events containing isolated leptons, missing transverse-momentum and a jet with a large transverse momentum. Top-quark decays into a jet from the hadronization of a bottom-quark and a $W$-boson are considered in the case where the $W$-boson decays hadronically. Events where a jet in the final-state contains a muon are also considered. No excess above the Standard Model expectation is found in either channel. An upper limit on the cross section for single-top production is established and it is found that this upper limit cannot rule out the hypothesis that the isolated lepton events are the product of single-top decays. Furthermore, an upper limit on the anomalous $\gamma - u - t$ coupling is established in the framework of recent NLO calculations. The sensitivity of HERA to flavour-changing neutral-current reactions is found to be competitive with that at other high energy colliders.

For my mum and dad.

*"Do you believe then that the sciences would ever have arisen and become great if there had not beforehand been magicians, alchemists, astrologers, and wizards who thirsted and hungered after abscondite and forbidden powers?"*

**Friedrich Nietzsche, 1886**

*"Just because some of us can read and write and do a little math, that doesn't mean we deserve to conquer the universe."*

**Kurt Vonnegut,** Hocus Pocus

# Contents

**1 H1 Experiment** **16**

1.1 The HERA *ep* Storage Facility . . . . . 16

1.2 An Overview of the H1 Detector . . . . . 18

1.3 Tracking Systems . . . . . 21

1.3.1 Forward Track Detectors . . . . . 21

1.3.2 Central Track Detectors . . . . . 23

1.3.3 Central $z$-chambers . . . . . 25

1.3.4 The Silicon Trackers . . . . . 25

1.3.5 The Backward Drift Chamber . . . . . 26

1.3.6 Multi-Wire Proportional Chambers . . . . . 26

1.4 Calorimetry . . . . . 27

1.4.1 The Liquid Argon Calorimeter . . . . . 28

1.4.2 The Backward Calorimeter . . . . . 30

1.4.3 The Tail Catcher . . . . . 31

1.4.4 The Plug Calorimeter . . . . . 31
1.5 Muon Detectors . . . . . 32
1.5.1 Instrumented Iron . . . . . 32
1.5.2 Forward Muon Detector . . . . . 32
1.6 Time of Flight Counters . . . . . 33
1.7 Luminosity Systems . . . . . 34
1.8 Triggering and Data Acquisition . . . . . 35

**2 HERA Physics** **38**

2.1 HERA Kinematics . . . . . 38
2.2 Deep Inelastic Scattering (DIS) . . . . . 40
2.3 Quantum Chromodynamics . . . . . 44
2.3.1 The Strong Coupling Constant . . . . . 44
2.3.2 QCD Factorisation . . . . . 46
2.3.3 DGLAP . . . . . 47
2.4 Photoproduction Physics . . . . . 47
2.4.1 Low $P_T$ Interactions . . . . . 48
2.4.2 High $P_T$ Interactions . . . . . 48
2.5 The Top-Quark . . . . . 51
2.5.1 The Top-Quark at HERA . . . . . 53

**3 Monte Carlo Event Generators** **58**

3.1 Hadronization Models . . . . . 59

3.1.1 String Fragmentation . . . . . 59

3.1.2 Cluster Hadronization . . . . . 59

3.2 PYTHIA - Photoproduction Event Generator . . . . . 60

3.3 HERWIG - Photoproduction Event Generator . . . . . 61

3.4 RAPGAP - DIS Event Generator . . . . . 61

3.5 EPVEC - Heavy Particle Decay Event Generator . . . . . 62

3.6 ANOTOP - Anomalous Single-Top Event Generator . . . . . 62

3.7 Predictions of QCD-based Models after Detector Smearing . . 63

**4 Jet Algorithms** **64**

4.1 Infra-red and Collinear safety . . . . . 65

4.2 Jet Algorithms . . . . . 66

4.3 Recombination Schemes . . . . . 67

4.4 Inclusive $k_T$ Algorithm . . . . . 67

4.5 The Cone Algorithm . . . . . 69

**5 Event Selection** **72**

5.1 Data Sets . . . . . 73

5.2 Selection of Multi-jet Events . . . . . 74

5.3 Subtriggers . . . . . 75

5.4 Reconstruction of the Hadronic Final-State . . . . . 76
5.4.1 Jet-Finding and Calibration . . . . . 78
5.5 High Transverse-Momentum Jet Selection . . . . . 79
5.6 Distributions of the Final-State . . . . . 81
5.6.1 Figure 5.3 . . . . . 82
5.6.2 Figure 5.4 . . . . . 84
5.6.3 Figure 5.5 . . . . . 84
5.6.4 Figures 5.6 . . . . . 86
5.7 Final Selection . . . . . 88
5.7.1 Discriminating Variables . . . . . 90
5.7.2 Muon Selection . . . . . 92
5.7.3 Final Top Selection . . . . . 97

**6 Systematic Errors** **101**

6.1 Hadronic Energy Scale . . . . . 101
6.2 QCD Model Uncertainty . . . . . 102
6.3 Uncertainty of Top-Quark Mass . . . . . 102
6.4 Luminosity . . . . . 103

**7 Results of the Single-Top Search** **104**

7.1 Upper Limit on the Single-Top Cross-section . . . . . 105
7.2 Isolated Lepton Events . . . . . 106

7.3 Extraction of the Anomalous Coupling . . . . . 107

**8 Conclusion** **109**

8.1 Future Prospects . . . . . 112

**A Derivation of Limits** **114**

A.1 Including Systematic Uncertainties . . . . . 117

# Acknowledgements

I would like to thank Professor Erwin Gabathuler, who gave me the opportunity to study for a Ph.D. at the University of Liverpool, and my supervisor Dr Tim Greenshaw.

Thanks to all the people who proof-read this thesis in its many forms and zealously cleansed it of errors. Dave Milstead, Erwin Gabathuler, Steve Maxfield and Tim Greenshaw, thnak you.

While out in Hamburg, I had the good fortune to work with very many talented and interesting people. Particular thanks go to Andrew Mehta for pointing my frantically pedalling brain in the right direction and making sure my stabilisers didn't fall off. Thanks also to Cristinel Diaconu and Terry Sloan with whom I worked directly. They have, at the very least, been subjected to more of my talks than any other living human beings and in this respect are a testament to the strength of the human spirit in adversity. Eram Rizvi, Beate Heinemann, Nick Malden, and others whom I have no doubt forgotten, get an honourable mention for answering my questions with a straight face.

Thanks also to those who have completely failed to keep a straight face. Andy

'Bleeding Edge' Washbrook, Dave 'Where Did That Pint Go?' Payne and Mark 'Catch Phrase' Tobin, whether in the office or in the pub or just trying to negotiate the release of a kebab in the special language of the very drunk, it's been a laugh. Paul 'Basset Hound' Laycock and Dave '24 hours' South made Hamburg a really very enjoyable place to be and it is fair to say that without them I would be far less familiar with the stations at Poppenbuttel and Wedel than I am.

Special thanks and love go to Steph, for an almost infinite amount of love, support *et tartines*.

And finally, I would like to thank my parents to whom this thesis is dedicated.

Thank you all.

The first three years of this PhD were funded by PPARC, the Particle Physics and Astronomy Research Council.

# The Author's Contribution

The author was responsible for developing the algorithms outlined in this thesis which select candidate events containing singly-produced top-quarks. Furthermore, the author performed the first such search at HERA. The author contributed to the operation of the H1 detector by acting as a data-taking shiftee and as an on-call high voltage expert for the H1 Forward Track Detector. The author also had responsibility for performing offline quality checks of the recorded data.

# Introduction

HERA, the Hadron Electron Ring Anlage, situated in Hamburg, is the only electron-proton collider facility in the world. The structure of the proton has been measured there across a previously inaccessible kinematic range covering decades in $x$ and $Q^2$. The high centre of mass energy at HERA ($\sim 320\,\mathrm{GeV}$) means that it is a promising place to look for heavy particle production. Such interactions are made possible when the probing photon from the electron strikes a constituent of the proton that carries a large fraction of the momentum of the proton.

The top-quark, discovered in 1995 by the CDF and D0 experiments at FERMILAB [1, 2], is without doubt a heavy particle. Its mass of $174\,\mathrm{GeV}$ makes it the heaviest of the known quarks and it is about 35 times more massive than its electroweak isospin partner the bottom-quark. Together with the bottom-quark the top-quark completes the third generation of quarks. In the Standard Model the top-quark decays rapidly and almost exclusively via $t \to Wb$, as already confirmed by experiment [3].

Although not kinematically forbidden, the production rate of single top-quarks in $ep$ collisions at HERA energies is negligible in the Standard Model

[4]. Flavour-Changing Neutral-Current, FCNC, interactions where, for example, an up-quark from the proton interacts with a photon to produce a top-quark, are not possible in the Standard Model at leading order. These processes arise only via higher order corrections and their consequent low rates make FCNC interactions an ideal place to look for new physics. A number of extensions to the Standard Model that produce sizeable FCNC interactions involving the top-quark have been proposed, for example, Standard Model-like models with an extended Higgs sector [5], supersymmetry [6], dynamical breaking of the electroweak symmetry [7] or additional symmetries [8].

Since full HERA operation began, an excess of events characterised by a high transverse-momentum lepton together with a large missing transverse-momentum has been observed. The observation of one such event in 1994 [9] was remarkable enough to warrant publication in its own right, and at the time of writing eighteen such events have been observed [10]. What makes these events particularly interesting is that they are occurring at a frequency far higher than the expected Standard Model rate, which is dominated by the $W$ production process

$$ep \rightarrow eXW \rightarrow eXl\overline{\nu_l}.$$

As well as containing a high-momentum lepton and missing momentum, attributed to the neutrino, these events are characterised by an hadronic system $X$, which is defined by all the reconstructed particles in the event save for the isolated leptons. As harsher and harsher cuts are made on the transverse-

| Transverse-Momentum of Hadronic System | Data | SM expectation |
|---|---|---|
| $p_T^X > 0$ GeV | 18 | $10.48 \pm 2.53$ |
| $p_T^X > 12$ GeV | 13 | $5.14 \pm 1.31$ |
| $p_T^X > 25$ GeV | 10 | $2.82 \pm 0.73$ |
| $p_T^X > 40$ GeV | 6 | $0.99 \pm 0.28$ |

Table 1: Observed and predicted event rates in muon and electron channels combined for all $e^+p$ data.

momentum, $p_T^X$, of this hadronic system the observed excess becomes more and more marked as shown in Table 1.

A possible origin for these events is single-top production via the FCNC reaction

$$ep \rightarrow eXt \rightarrow eXWb \rightarrow eXl\overline{\nu_l}b.$$

This reaction would enhance the $W$-boson cross section and the hadronic final-state of the event would contain a high transverse-momentum jet coming from the hadronization of the bottom-quark. This would naturally explain the observed excess at high values of $p_T^X$. However, an independent check must be made in order to confirm that the observed events are the product of single-top production.

The analysis presented in this thesis is dedicated to the search for evidence of the process

$$ep \rightarrow eXt \rightarrow eXWb \rightarrow eXqq'b$$

where the $W$-boson decays hadronically. If the excess in the leptonic channel is due to single-top production, then a similar excess would appear in this fully hadronic channel thus confirming the hypothesis. In the absence of a definite signal the results can be used to set an upper limit on the cross-

section for single-top production. Events of this type typically contain three or more high transverse-momentum jets from the hadronization of the two quarks from the decay of the $W$-boson and one jet from the hadronization of the bottom-quark. The background to this signal comes mainly from electro- and photo- production of high transverse-momentum jets.

The first chapter of this thesis gives a general overview of the H1 detector along with more detailed information concerning the systems of direct relevance to this analysis. Chapter 2 deals with HERA physics and theoretical aspects of both single-top production, and the expected background processes. Chapter 3 outlines how the various theories are implemented via Monte-Carlo based event generators. Chapter 4 describes the jet algorithm used in this analysis. Chapter 5 details the event selection and shows how top-quark events can be separated from the background. Chapter 6 details the systematic uncertainties present in this analysis and Chapter 7 gives the results obtained and uses these to derive a limit on single-top production and the anomalous coupling. The final chapter provides the conclusion and summary of the work.

# Chapter 1

# H1 Experiment

The H1 experiment [11, 12] is to be found at HERA [13], the Hadron Electron Ring Anlage; to date, the only electron[1]-proton collider in the world. In operation since 1992, the H1 detector has been used to study electron-proton and positron-proton scattering over a wide and previously inaccessible kinematic range. In this chapter, an overview of the HERA accelerator is presented. This is followed by a detailed description of the H1 experiment and the subdetectors relevant to this analysis.

## 1.1 The HERA *ep* Storage Facility

Situated beneath the leafy western suburbs of Hamburg in a near-circular tunnel 6.3 km long, HERA consists of two beampipes in which electrons at

[1]Since HERA can run with either positrons or electrons, and in order to avoid the use of cumbersome compound phrases like positron/electron, the term electron will be used to refer to both electrons and positrons unless the distinction is made explicit in the text.

an energy of 27.5 GeV and protons at an energy of 920 GeV are circulated clockwise and anti-clockwise, respectively. These counter-circulating beams are steered to make collisions at two locations known as the North and South Halls. The H1 experiment is situated in the North Hall and the ZEUS experiment in the South Hall. The centre of mass energy at the interaction points is approximately 320 GeV and the asymmetric beam energies have consequences for the detector designs.

Each beam is composed of discrete bunches of particles separated by 96 ns gaps. A maximum of 220 bunches can be stored at any one time and these lead to maximum electron and proton beam currents of $\sim 30$ mA and $\sim 100$ mA respectively. The electron bunches conform to an approximately Gaussian longitudinal distribution, but the shape of the proton bunches is complicated by "satellite" bunches which appear at 5 ns intervals and arise from protons escaping into adjacent radio frequency "buckets" during injection into HERA. The bunches are further subdivided into colliding and non-colliding, or pilot bunches. In colliding bunches, an electron bunch is paired off with a proton bunch for collision. The pilot bunches have no partner in the other beam and are used to determine background levels from "beam-gas" and "beam-wall" interactions. In a beam-gas interaction, a proton or electron interacts with residual gas in the beam pipe. In a beam-wall interaction, particles from the beam interact with the beampipe itself.

In addition to the two colliding-beam experiments there are also two fixed target experiments, HERMES and HERA-B; the former uses only the electron beam and the latter only the proton beam. In the HERMES detector

the longitudinally polarised electron beam collides with a polarised hydrogen, deuterium or helium gas target. The aim of the experiment is to measure the spin structure of the nucleons. HERA-B is a large-aperture high-rate spectrometer built for studies of collisions of protons with the nuclei of target wires positioned in the halo of the HERA proton beam. From 2002 onwards HERA-B will be devoted to measurements of the atomic-number dependence of charmonium production and a measurement of the B-production cross section at 920 GeV.

Since the start of operation, HERA has provided a steadily increasing luminosity. Between 1994 and 1997, running with positrons, HERA delivered $63\,\mathrm{pb}^{-1}$ of luminosity. In the $1999-2000$ period HERA delivered $95\,\mathrm{pb}^{-1}$ and was operating at design luminosity [14].

## 1.2 An Overview of the H1 Detector

A detailed description of the H1 detector can be found in reference [11, 12]. The components relevant to this analysis are discussed below. A schematic cut-away diagram of the H1 detector is shown in Figure 1.1. This device is used to study the properties of elementary particles produced in high-energy electron-proton collisions. A series of tracking (2 and 3) and calorimetric (4, 5, 10, 12 and 13) detectors provide almost hermetic coverage around the interaction point. However, the beam pipe and beam magnets (1) cause an unfortunate blind spot. In addition there are two systems, which are designed primarily to detect muons (9). Due to the asymmetry of the beam

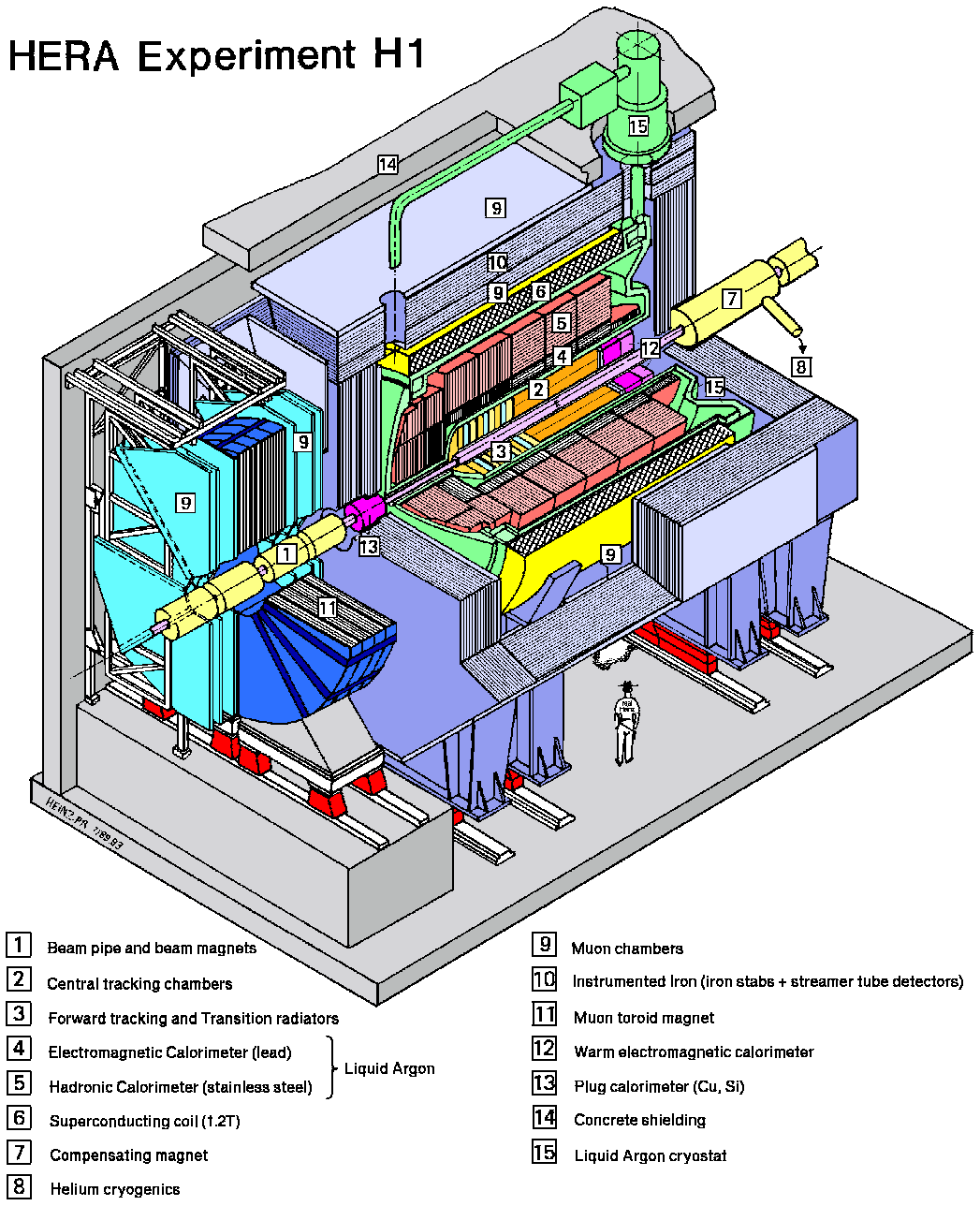


Figure 1.1: A Schematic of the H1 Detector showing all subdetectors.

energies, the majority of particles produced in the interactions are boosted in the proton-beam direction and the instrumentation is therefore concentrated in this region, which is referred to as the "forward" region of the detector.

Points within the detector are defined using Cartesian coordinates with respect to an origin chosen to be the nominal interaction vertex. The positive $z$-direction is parallel to the proton beam direction through the detector. The $y$-direction is vertically upwards and the $x$-direction points towards the centre of the HERA ring. Thus the "forward" region described above corresponds to the positive $z$-direction. A spherical-polar coordinate system is more natural for studying particles originating at a single point and the convention assumed is that the polar angle, $\theta$, is measured from the positive $z$-axis and that the azimuthal angle, $\phi$, is defined as the angle in the $x - y$ plane as measured from the $x$-axis. Another useful angular measure is the pseudo-rapidity which is defined as

$$\eta = -\ln \tan \frac{\theta}{2} \tag{1.1}$$

This variable has the benefit that differences in $\eta$ are invariant under longitudinal boosts, i.e. boosts along the $z$-axis.

In the following sections the components of the H1 detector are described starting from the interaction point.

## 1.3 Tracking Systems

The trackers in H1, shown in Figure 1.2, fall into two major categories: drift chambers and multi-wire proportional chambers (MWPC). Drift chambers provide accurate positional information at resolutions of order 100 $\mu$m, but, due to the relatively large drift times (up to around 1 $\mu$s) that are an inherent feature of their design, the timing information they supply is not prompt enough for the needs of fast triggering, which should ideally be faster than the time for one bunch-crossing, 96 ns. This weakness is compensated for by the MWPCs, which, on the one hand provide prompt timing information (typically within 20 ns) for triggering, but on the other hand poorer spatial resolution.

The H1 tracking systems is divided into three regions: the forward, central and backward regions. The trackers sit in a 1.15 T solenoidal magnetic field that causes the paths of charged particles to curve allowing their momenta to be measured.

### 1.3.1 Forward Track Detectors

In the forward region there is only one tracker, the Forward Track Detector (FTD). This consists of three identical supermodules, each supermodule comprising a planar module, a proportional chamber, a passive transition radiator and a radial module. The radial and planar drift chambers that make up the radial and planar modules have different wire geometries. In the planar drift chambers, the wires are parallel to one another and perpen-

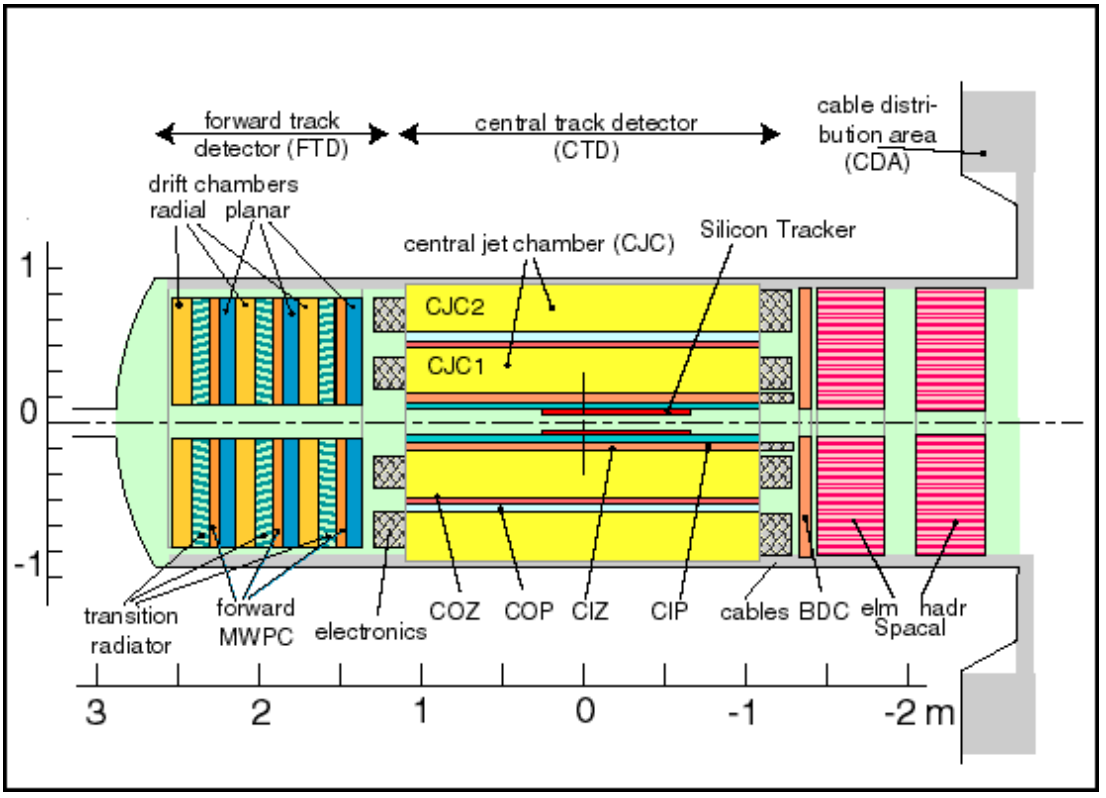


Figure 1.2: A Schematic of the H1 tracking detectors.

dicular to the beam direction. In the radial drift chambers, the wires are strung radially and perpendicular to the beam direction.

The planar module consists of three planar drift chambers, each four wires deep in $z$ and rotated at 60° to each other in azimuth. The proportional chamber is mounted directly behind the planar drift chambers in order to share the same gas mixture and maximise the geometrical trigger efficiency of the FTD. After the proportional chamber the particles traverse a transition radiator consisting of 400 polypropylene foils contained in its own gas volume. Transition radiation photons pass through a thin mylar window and are detected in the radial chamber. To improve double track resolution the second and third radial modules are rotated by 3.75° and 2.5° relative to the first. The interleaving of planar and radial chambers provides the optimum lever arm for momentum measurement. The FTD covers an angular range of $7° < \theta < 25°$ and has a momentum resolution of $\sigma_p/p^2 < 0.03\,\mathrm{GeV}^{-1}$ and a track angular resolution of $\sigma_{\theta,\phi} < 1\,\mathrm{mrad}$ [15].

### 1.3.2 Central Track Detectors

The main trackers in the central region are the Central Jet Chambers (CJC1 and CJC2) [16]. The relative positions of these and the other H1 central trackers are shown in Figure 1.3 . They are arranged concentrically about the beam axis as shown in Figure 1.3. These detectors are formed from planar cells inclined at 30° with respect to the radial direction. The sense wires in each planar cell are arranged in planes parallel to the $z$-axis. Each of the cells in the CJC1(2) contains 24(32) sense wires. There are 30(60) drift

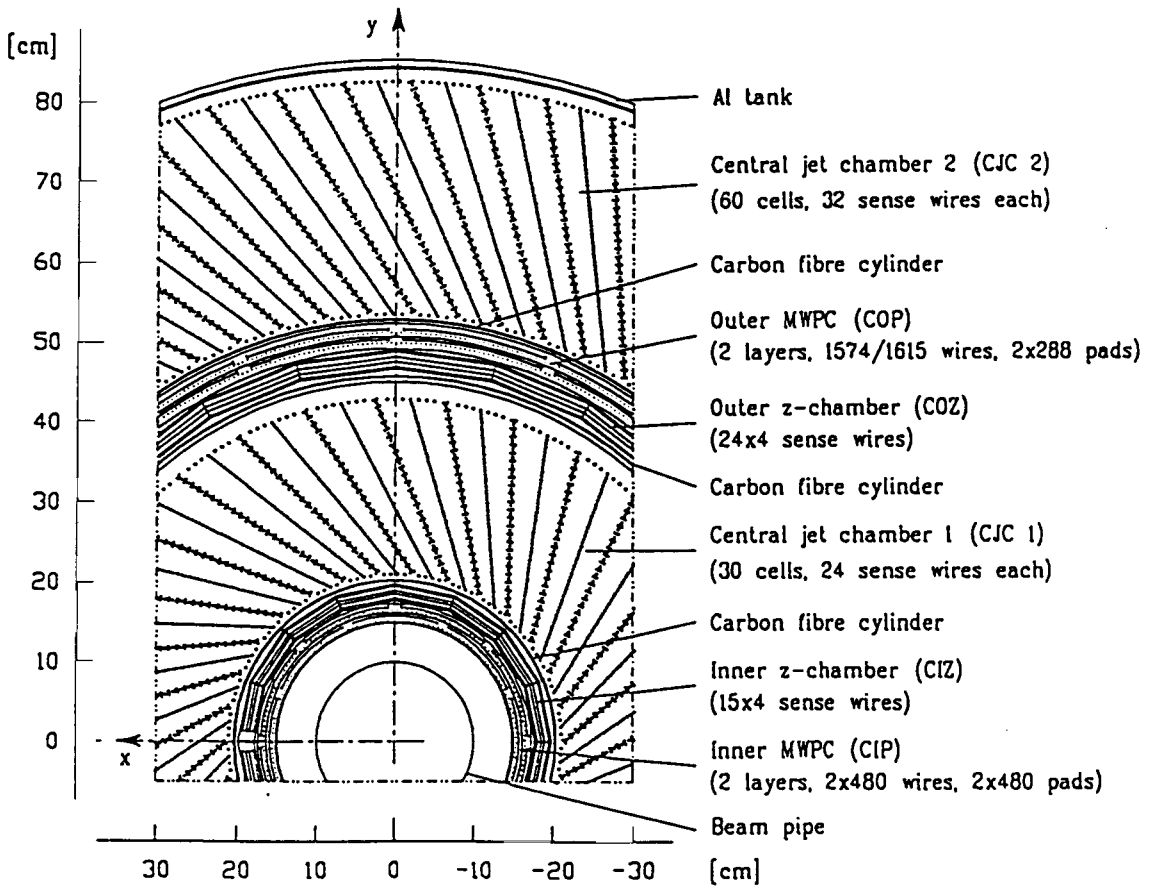


Figure 1.3: H1 Central Trackers

cells. This geometry has the advantage that high momentum tracks will cross more than one cell thus improving the track resolution. It also eliminates the usual drift chamber ambiguity since wrong track segments will not point to the event vertex and will not match segments in neighbouring cells. The CJC's provide a resolution in the $r - \phi$ plane of $\sim 170\,\mu$m, from drift time measurements, but because the sense wires are strung parallel to the $z$-axis and the $z$-coordinate measurement comes from charge division techniques the $z$-resolution is limited to $\sim 2.2\,$cm [17].

### 1.3.3 Central $z$-chambers

The relatively poor $z$-resolution of the CJC's is compensated for by the Central Inner and Central Outer $z$-Chambers (CIZ and COZ). Their relative positions are shown in figure 1.3. In these drift chambers the sense wires are strung azimuthally with the electric field in the cells aligned in the $z$-direction to ensure accurate measurement from drift times of the $z$-coordinate. The precision achieved is $\sim 300\,\mu$m. In the $\phi$ coordinate the resolution from charge division is $\sim 2\%$ of $2\pi$ [18, 19].

### 1.3.4 The Silicon Trackers

The backward silicon tracker (BST) was installed in 1995 and gradually upgraded each year. The BST consists of four detector planes, arranged perpendicularly to the beam axis which are equipped with 16 wedge-shaped, double-metal silicon-strip detectors. The BST measures the polar angle of

tracks with an internal resolution of about 0.2 mrad from radial coordinates between 5.9 cm and 12.0 cm [20]. In 1996, the central silicon tracker (CST) was installed. This device comprises two layers of silicon-strip detectors and covers a polar acceptance of $30° < \theta < 150°$, $2.0 < \eta < -2.0$. The achieved resolution in distance of closest approach of tracks with hits in both CST layers is given by $\sigma_{dca} \approx 40\,\mu\text{m} \oplus 100\,\mu\text{m}/\text{p}_\text{T}$ [GeV] [21].

### 1.3.5 The Backward Drift Chamber

The BDC was installed in 1995 and covers an angular region of $153° < \theta < 177.5°$ and is used primarily to improve the measurement of the angle of the scattered electron. The BDC consists of four double-layer, octagonal drift chambers mounted along the $z$-direction. The sense wires in each layer are strung in a similarly octagonal pattern such that the drift direction is more or less radial. Hit resolutions of 0.55 mm in the radial direction and 2.5 mm in the azimuthal direction have been achieved [22].

### 1.3.6 Multi-Wire Proportional Chambers

In addition to the drift chambers there are also a set of MWPC's that, in relation to the nominal interaction point, cover the entire solid angle between 5° and 175°. Their purpose is threefold. They deliver a fast timing signal with a time resolution better than the HERA bunch-crossing rate (96 ns). They provide space points for charged-particle track reconstruction and lastly they add an accurate track element in the backward direction where the

drift chambers fail to provide enough space points. In the forward region the forward proportional chambers (FPC) are interleaved between the drift chambers of the FTD. In the central region there are two MWPCs, the CIP and COP [23] standing for central inner and central outer proportional chambers respectively. The CIP lies closest to the interaction region and consequently covers the largest solid angle. In order to avoid degrading the track reconstruction ability of the neighbouring chambers, the CIP and COP are fabricated from low-mass materials. The time resolutions for the CIP, COP and the forward tracker's proportional chambers are all around 20 ns.

Until 1994 a backward proportion chamber (BPC) existed to augment the measurement of the polar angle of the scattered electron in the region $150^\circ < \theta < 173^\circ$, though this was replaced in 1995 by the backward drift chamber (BDC).

## 1.4 Calorimetry

There are four main calorimeters in the H1 detector. The Liquid Argon Calorimeter (LAC) is the main calorimeter used for the detection of the hadronic final-state and also for electron identification in high-$Q^2$ events. It covers the central part of the detector between $4^\circ < \theta < 154^\circ$. The SPACAL, a spaghetti calorimeter, is located in the backward region and its main use is in electron identification although it has a hadronic section that allows the detection of backward jets. There are two other systems: the PLUG calorimeter, which closes the gap between the LAC and the beampipe in the

forward direction with copper absorbers and silicon pad readout at angles between $0.3^\circ < \theta < 4^\circ$, and the Tail Catcher. The latter, incorporated into the iron return yoke of the magnet, measures energy leakage from the main calorimeters and is used for muon detection.

### 1.4.1 The Liquid Argon Calorimeter

The Liquid Argon Calorimeter (LAC) [24] is a sampling calorimeter composed of electro-magnetic (EMC) and hadronic parts (HAC). To reduce the amount of dead material encountered by particles before they reach the calorimeter the LAC is wholly contained within the solenoid magnet. In addition to being separated into EMC and HAC sections, the LAC is further divided into 8 wheels in $z$, each of which is divided into either 6 or 8 octants. A schematic diagram of the LAC, showing the relative shapes and positions of these wheels, is shown in Figure 1.4. These provide complete azimuthal coverage and cover a range in polar angle of $4^\circ < \theta < 154^\circ$.

The active (sampling) material for both the EMC and HAC is liquid argon chosen for its high atomic density which leads to large ionization. The passive (absorbing) layers are provided by 2.4 mm thick lead plates in the EMC and 16 mm thick stainless steel plates in the HAC. The difference in thickness allows for the relative length scales of electro-magnetic and hadronic shower development. The difference in character of the shower development also leads to a difference in the fraction of energy actually detected from hadronic and electro-magnetic showers. The calorimeter is non-compensating. Typically, the energy response to hadronic particles is about 30% lower than the

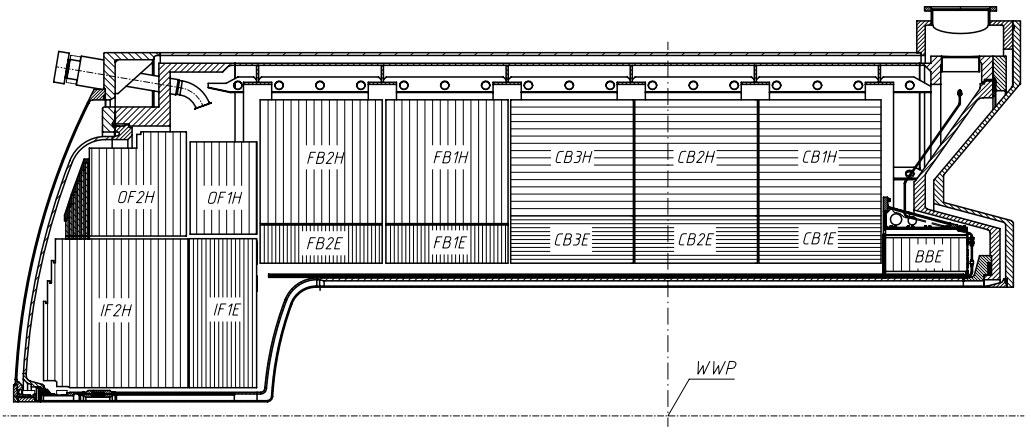


Figure 1.4: Transverse section of the Liquid Argon Calorimeter showing the disposition of the various wheels

response to electro-magnetic particles. To account for this a correction is applied to the reconstruction of hadronic showers. The thickness and degree of instrumentation of the calorimeter vary across the angular range to account for the difference in expected distribution of particles owing to the asymmetric beam energies. Charge deposited from ionization in the LAr cells is collected on cathode pads and read out in a total of 45000 channels. The EMC and HAC channels are combined into 256 'towers' built so as to point back to the nominal vertex. The transverse-momentum and energy in these towers are summed and provide the basis for LAC triggering. The granularity of the cells is arranged such that the resolution is approximately uniform in laboratory pseudo-rapidity.

After calibration, carried out using test-beam facilities [25] and cross-checked *in situ*, the calorimeter has been shown to have an energy resolution of $\frac{\sigma_{EM}(E)}{E} \approx \frac{0.15}{\sqrt{E/\mathrm{GeV}}} \oplus 0.01$ for electrons, and $\frac{\sigma_{HAD}(E)}{E} \approx \frac{0.5}{\sqrt{E/\mathrm{GeV}}} \oplus 0.02$ for charged pions. The absolute energy scale is known to between 0.7% and 3%

(depending on the wheel) for the EMC and to 4% for the HAC [26].

### 1.4.2 The Backward Calorimeter

In 1994 the backward electromagnetic lead-scintillator calorimeter (BEMC) was used to measure the properties of the scattered electron for polar angles in the range $155° < \theta < 176°$. An energy resolution of $0.1/\sqrt{E_e/\mathrm{GeV}} \oplus 0.42/E_e/\mathrm{GeV} \oplus 0.03$ was achieved [27]. The absolute electromagnetic scale was determined to a precision of 1% [28]. Since it consisted of only one interaction length of material, the hadronic response of the BEMC was poor and approximately 30% of incident hadrons left no significant energy deposition. Consequently, a large scale uncertainty of 20% exists for hadronic measurements made with this device.

In 1995, the BEMC was replaced by the SPACAL [29]. This is a SPAghetti CALorimeter that covers an angular range of $153° < \theta < 177.5°$. Its primary use is the identification of electrons, but it also has an hadronic section that allows the detection of jets in the backward region.

The SPACAL consists of lead sheets in which scintillating fibres (the spaghetti) are embedded. Particles shower in the lead causing the fibres to scintillate. The light is then collected by Photo-Multiplier Tubes (PMT's), converted into an electric pulse and read out. The active volume of the electro-magnetic section is 25 cm deep with a lead-to-fibre ratio of 2.3 : 1, corresponding to 28 radiation lengths. The hadronic section is only one interaction length deep and has a lead-to-fibre ratio of 3.4 : 1.

Test-beam results are consistent with an energy resolution of $\frac{\sigma_E}{E} \approx \frac{0.7}{\sqrt{E/\mathrm{GeV}}} \oplus 0.01$ in the electro-magnetic section and a hadronic energy resolution of $\frac{\sigma_E}{E} \approx \frac{0.56}{\sqrt{E/\mathrm{GeV}}} \oplus 0.03$ [29]. The overall energy scales of the hadronic and electromagnetic sections are known to within 1% and 7% respectively [30].

In 1999, the Very Low $Q^2$ (VLQ) calorimeter was installed. This is a tungsten-scintillator strip calorimeter designed to measure the scattered electron in the angular range $177^\circ < \theta < 179.4^\circ$. An electromagnetic energy resolution of approximately $0.19/\sqrt{E/\mathrm{GeV}}$ has been achieved [31].

### 1.4.3 The Tail Catcher

The iron of the return yolk is instrumented with layers of Limited Streamer Tubes (LST's) that allow for a coarse measurement of the energy of hadronic showers not fully contained by the other calorimeters. It also functions as a muon detector. The iron is divided into three sections (central barrel, and forward and backward endcaps) each of which has 16 layers of LST's. The energy resolution is $\frac{1}{\sqrt{E/\mathrm{GeV}}}$ with a scale uncertainty of $\sim 35\%$.

### 1.4.4 The Plug Calorimeter

The PLUG calorimeter covers the range $0.3^\circ < \theta < 4^\circ$, fitting neatly between the LAC and the beampipe in the forward direction. It is composed of layers of copper and sampling layers of silicon. Due to incomplete shower containment and the coarse sampling used, the energy resolution is estimated from experiment-supported Monte-Carlo calculations [32] to be $\frac{1.50}{\sqrt{E/\mathrm{GeV}}}$.

## 1.5 Muon Detectors

### 1.5.1 Instrumented Iron

The return yoke of the magnet, used in the tail catcher, is also used to detect muons. The central muon system consists of an octagonal barrel and is terminated with two flat endcaps giving an angular coverage from $4° < \theta < 170°$. It is further divided into 64 modules each of which is built up in a sandwich structure with 10 iron plates of 7.5 cm thickness and layers of Limited Streamer Tubes.

### 1.5.2 Forward Muon Detector

To aid the identification of muons in the very forward region there is an additional system, the Forward Muon Detector (FMD) [33]. It is located outside the iron return yoke and covers the angular range in $\theta$ from 3° to 17°.

The FMD is built up from six double layers of drift chambers four of which have their sense wires strung tangentially around the beampipe for measuring $\theta$ and two of which are strung radially in order to provide an improved $\phi$ measurement. The six layers are divided into two groups of three separated by a toroidal magnet. This magnet is designed to allow momentum measurements in the range $5\,\mathrm{GeV} < \mathrm{p} < 100\,\mathrm{GeV}$. The lower limit is due to the amount of material a muon must traverse between the interaction point and the FMD and the influence on the momentum resolution from multiple-coulomb scattering in the iron of the magnet. The upper limit is set by the

field strength of the toroid and the resolution of the drift chambers. The spatial resolution of the drift cells is $\sim 250\,\mu$m from drift time measurement and $\sim 4\,$cm from charge division measurement along a wire. The momentum resolution varies from 24% at 5 GeV to 36% at 200 GeV.

The double layers are staggered with respect to one another in order to improve efficiency and resolve the ambiguity that arises from not knowing, in a single layer, on which side of the sense wires a particle has passed. Pairs of hits in the double layers are linked to those in the other modules on the same side of the toroid to form track segments and then full tracks are reconstructed by linking these segments across the toroid.

## 1.6 Time of Flight Counters

Accurate timing measurements are a very effective way of reducing the large non-*ep* backgrounds caused by beam-gas and beam-wall interactions. Timing measurements with an accuracy of a few nanoseconds are provided by scintillators placed at +790 cm, +540 cm, −275 cm, −650 cm and −810 cm. Beam-gas and beam-wall interactions are detected in the scintillators at roughly the same time as the proton bunch passes through. Electron-proton events centred on the nominal vertex, however, result in particles being detected $\sim \frac{2\Delta z}{c}$ later, where $\Delta z$ is here the displacement of the scintillator from the nominal interaction vertex. This delay corresponds to a time difference of $\sim 13\,$ns for the ToF system at −275 cm and of $\sim 22\,$ns and $\sim 27\,$ns for the veto walls at −650 cm and −810 cm [34, 35].

## 1.7 Luminosity Systems

The luminosity system of H1 serves a number of purposes. Its main task is to provide a fast luminosity measurement. It also provides electron-beam monitoring for the HERA machine and an absolute luminosity measurement in the interaction region. Furthermore, it is used to tag photoproduction interactions via an energy measurement for electrons scattered under small angles. Photons produced in initial-state radiation are also measured.

The luminosity measurement is based on the precisely calculated QED Bethe-Heitler process; $ep \to ep\gamma$ [36]. The main source of background is bremsstrahlung from the residual gas in the beampipe, $eA \to eA\gamma$. At design luminosity these events are expected at 10% of the $ep \to ep\gamma$ rate, but can be subtracted using data from the electron pilot bunches. The hardware system consists of a Photon Detector (PD) and an Electron Tagger (ET). The on-line measurement of luminosity is based on coincident hits in both these systems. The angular distributions for both the scattered electron and the photon are strongly peaked in the direction of the electron beam. The detectors must therefore be placed close to the beam pipe and far from the interaction region in order to cover these small angles. The photon tagger is located at $z = -103\,\mathrm{m}$ and there are electron taggers at $z = -33\,\mathrm{m}$ and $z = -44\,\mathrm{m}$. The taggers are all crystal calorimeters. The photon detector is a $5 \times 5$ array of crystals and the electron taggers are $7 \times 7$ arrays.

Off-line, the luminosity measurement is calculated from the rate of scattered photons only. Corrections are also made to this value that take into account the amount of luminosity contained in the proton bunch satellites. The

satellites can contribute up to 10% of the proton current.

## 1.8 Triggering and Data Acquisition

There are two major challenges to the detection and recording of *ep* events in H1. The first is that the rate of background events is typically $\sim 10^3$ times the rate for interesting *ep* events, and the second is that the time between bunch-crossings of 96 ns is much shorter than the time needed to readout fully and permanently store an event. These two problems are surmounted by a multi-level trigger system as detailed below.

Almost all of the H1 subdetectors contain at least one trigger system. At each bunch-crossing these send out eight bits of information to the central trigger. These eight bits constitute a trigger element, which must arrive within 22 bunch-crossings of the event. This delay is set by the response time of the slowest system, in this case the LAC. The central trigger then takes the trigger elements and makes a decision on the quality of the event within the next two bunch-crossings. During the 24 bunch-crossings it takes to gather all the information and make this decision, the information for this and subsequent events is stored in a pipeline. If at this point the event is rejected, it is shunted off the end of the pipeline by the arrival of the next event. However, if the central trigger accepts the event, the information from the correct crossing is read out. Pipelining the events in this way ensures that the first-level trigger is dead-time free, where dead-time is defined as the time in which the read-out electronics are unable to accept new events. The

central trigger reaches its decision as to whether or not an event is of interest by making logical combinations of the trigger elements. These combinations are called subtriggers and there are currently 128 in use in H1. If at least one subtrigger is satisfied then the "L1 Keep" signal is sent. The subtriggers are designed mostly to combine background rejection with physics selection elements. In addition, there are many subtriggers used either to monitor specific background levels, or to calculate trigger efficiencies. Because these other elements are essentially physics triggers with relaxed conditions the rates for these triggers are relatively high. Because it is undesirable for these triggers to use a large amount of bandwidth, prescales are applied that in effect tell the central trigger to accept only some proportion of events that satisfy that subtrigger.

Dead time begins once an "L1 Keep" signal is received. This can be interrupted after 20 $\mu$s by a rejection from the level 2 (L2) trigger and the pipeline re-enabled. The L2 trigger is made up of two separate triggers, the topological trigger (L2TT) and the neural network trigger (L2NN). They make use of additional information from the trigger sub-systems to reconstruct the paths of particles. Use of additional L2 information allows prescale factors to be reduced for high-rate L1 subtriggers.

If an "L2 keep" signal is given, the full event information from all subdetectors is sent to the level-4 (L4) trigger. Dead-time ends when all information has been sent to the Central Event Builder (CEB) of L4 and the pipelines are re-enabled. The triggering and readout of an event amount to about $1 - 2$ ms of dead time. The level-4 trigger system consists of $\sim$ 30

power PCs and is capable of processing up to 30 events in parallel. At this point a limited reconstruction of the event is made and fast, often complex, on-line cuts are applied. The L4 trigger rejects the bulk of remaining beam-gas and cosmic backgrounds, as well as those resulting from trigger noise. If the rate of events input to L4 exceeds $\sim 50\,\mathrm{Hz}$ then dead time starts to accumulate from the reconstruction of events in the CEB. In normal running conditions the dead time is typically $\sim 10\%$. Events pass the L4 filter at a rate of $\sim 10\,\mathrm{Hz}$. In addition, $\sim 1\%$ of events that fail L4 are also passed in order to monitor the effects of the cuts. All data passing L4 are written to tape (typically 130 kbytes/event) and permanently stored.

Further selection takes place off-line to prepare the data sets for physics analysis. Full reconstruction and classification is carried out and is referred to as L5.

# Chapter 2

# HERA Physics

This chapter gives an overview of the physics of $ep$ collisions at HERA which is relevant to the search for hadronic decays of single top-quarks. This includes a review of the kinematic quantities generally used to characterize $ep$ interactions, a description of the photo-production, $\gamma p$, and deep-inelastic scattering, DIS, regimes and a discussion of photon and proton structure. Following this there is a brief outline of top-quark physics.

## 2.1 HERA Kinematics

In the Standard Model (SM) (see references [37, 38, 39, 40] for a polite introduction) of particle physics the interactions of electrons with protons are described by the exchange of gauge bosons. The boson couples to the electron and to a constituent parton in the proton as shown in Figure 2.1. In Figure 2.1 the interacting boson is a photon, but at HERA there are

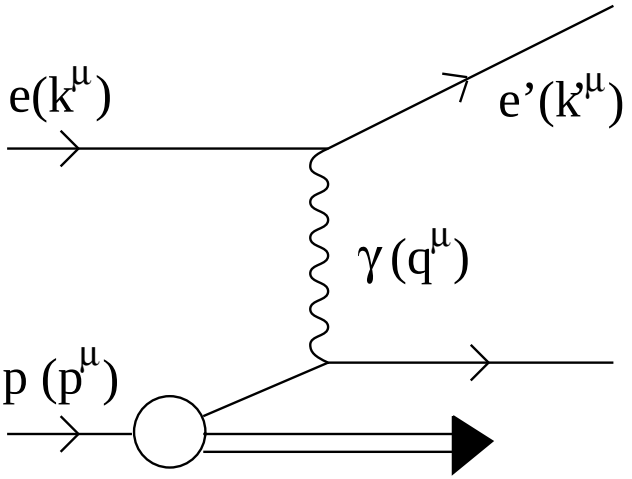


Figure 2.1: Diagram of a generic DIS process.

also interactions involving $Z$ and $W$ bosons. In the latter case the scattered electron $e'$ is replaced by an electron neutrino. The negative square of the four-momentum carried by the boson is known as $Q^2$ and is defined as

$$Q^2 = -q^2 = -(k - k')^2 \tag{2.1}$$

where $k$, $k'$, and $p$ are the four-momenta of the particles shown in Figure 2.1. Additionally two other important kinematic variables, Bjorken $x$ and Bjorken $y$, can be defined:

$$x = \frac{Q^2}{2p.q}, \; y = \frac{p.q}{p.k} \tag{2.2}$$

In the infinite momentum frame of the proton, and in the case when the struck parton is collinear with the proton, $x$ represents the fraction of the four-momentum of the proton that is carried by the struck parton. Similarly, $y$ can be thought of as the fraction of the momentum of the electron that is

carried by the photon. Both $x$ and $y$ run from zero to unity.

$Q^2$, $s$, $x$ and $y$ may be related via the centre of mass energy squared, $s$, (neglecting incoming particle masses) by

$$Q^2 = sxy \tag{2.3}$$

$Q^2$ has a useful physical interpretation. Via the uncertainty principle, $Q^2$ can be interpreted as the characteristic size scale of the interaction and, while the proton does not have a clearly defined radius, its size can be estimated from nuclear scattering experiments. The size of the proton determined in this way is of order $10^{-15}\,\mathrm{m}$ or, in natural units, $\sim 1\,\mathrm{GeV}$. This implies that, above a $Q^2$ value of approximately $1\,\mathrm{GeV}^2$, the virtual photon is able to probe the structure of the proton. This is the classic DIS scenario. For a $Q^2$ value $\ll 1\,\mathrm{GeV}^2$, however, the photon is not able to resolve the structure of the proton. This is the photoproduction, or $\gamma p$, regime. In the total $ep$ cross section there is a term that goes as $Q^{-4}$. This factor means that photoproduction dominates the HERA event rate.

Despite the fact that $Q^2$ is a continuous variable running smoothly from the DIS to the photoproduction regime, the way that the two are handled theoretically is quite distinct.

## 2.2 Deep Inelastic Scattering (DIS)

The scattering of an electron off a proton via the exchange of a virtual photon can be used to probe the structure of the proton. At lowest order in Quantum

Electro-Dynamics (QED) this scattering can be described in terms of two structure functions, $F_1(x, Q^2)$ and $F_2(x, Q^2)$. These structure functions are dependent on the distribution of electric charge in the proton. Using them the *ep* cross section can be written [41] in the following way

$$\frac{d^2\sigma_{ep\to eX}}{dxdQ^2} = \frac{4\pi\alpha_{em}^2}{xQ^4}\left[xy^2F_1\left(x,Q^2\right) + (1-y)\,F_2\left(x,Q^2\right)\right] \tag{2.4}$$

where $\alpha_{em}$ is the electro-magnetic fine-structure constant. The exchange of $Z^0$ bosons is suppressed at low $Q^2$ due to a term in the propagator proportional to the square of $\frac{Q^2}{Q^2+M_{Z^0}^2}$, where $M_{Z^0}$ is the mass of the $Z^0$ boson. When this term becomes non-negligible, i.e. when $Q^2 \geq M_{Z^0}^2$, a third parity-violating term, $F_3$, contributes to the cross-section. Its effect is negligible in the analysis presented in this thesis.

In the Quark-Parton Model (QPM) [42, 43], the proton is made up from non-interacting point-like quarks and the electron-proton interaction cross-section is approximated by an incoherent sum of elastic electron-parton cross-sections. In the QPM the structure functions $F_1$ and $F_2$ can be written in terms of the Parton Density Functions $f_i(x)$. These PDFs give the probability of finding a quark of type $i$ and charge $e_i$ carrying a fraction $x$ of the momentum of the proton. In this case,

$$F_1\left(x,Q^2\right) = \frac{1}{2}\sum e_i^2 f_i\left(x\right) \tag{2.5}$$

$$F_2\left(x,Q^2\right) = x\sum e_i^2 f_i\left(x\right) \tag{2.6}$$

and so $F_1$ and $F_2$ are related by the Callan-Gross [44] relation

$$F_2\left(x, Q^2\right) = 2xF_1\left(x, Q^2\right) \tag{2.7}$$

In the QPM the structure functions depend only on $x$. Therefore, for a fixed value of $x$ the cross-section should be independent of $Q^2$ [45]. Figure 2.2 shows a measurement of $F_2(x, Q^2)$ as a function of $Q^2$ for various values of $x$. Note that, although, at high $x$, $F_2\left(x, Q^2\right)$ shows the expected scale invariance, detailed measurements carried out at BCDMS [46]and H1 [47] reveal that a $Q^2$ dependence appears as $x$ falls.

One assumption made in the QPM is that the sum of the momenta of the quarks and antiquarks is equal to the total momentum of the proton. This assumption can be expressed by the sum rule:

$$\sum_i \int_0^1 x f_i\left(x\right) dx = 1 \tag{2.8}$$

When this integral is calculated experimentally, however, the total momentum carried by quarks is found to be only about half of the momentum of the proton [40, 41]. This effect and a number of others, including the non-observation of free quarks, the deviation from scale invariance and (contrarily) the success of the QPM at high-$x$ (see Figure 2.2), can be explained by Quantum Chromodynamics, QCD [38].

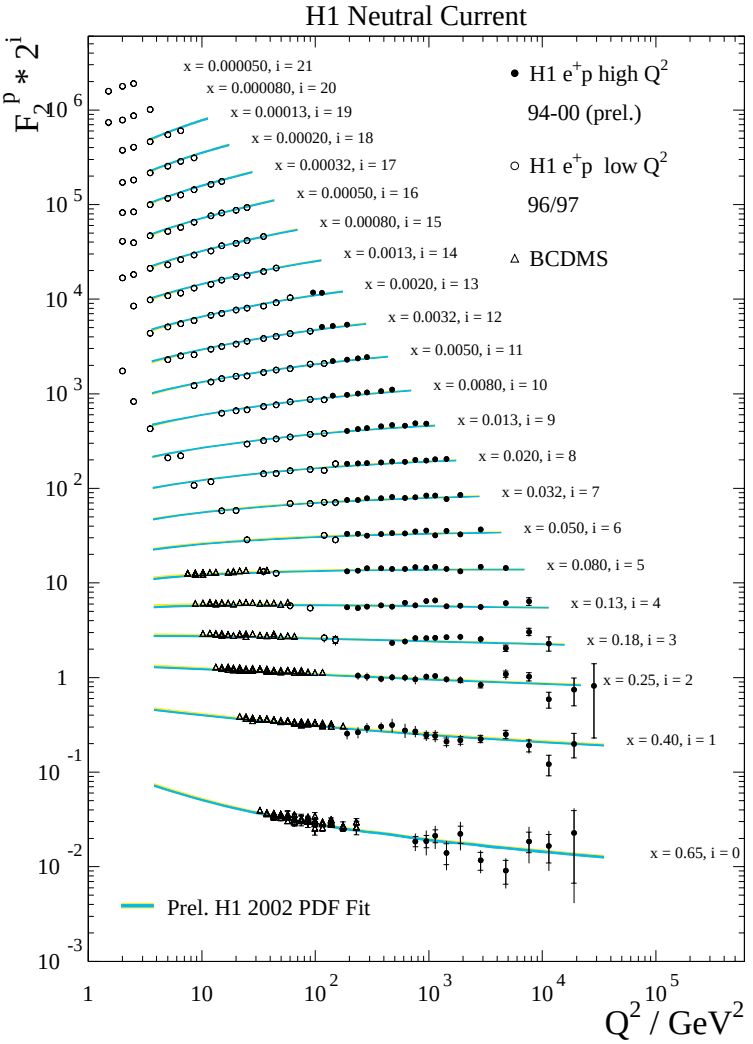


Figure 2.2: The proton structure function $F_2(x, Q^2)$ from H1 data compared to the preliminary H1 2002 PDF Fit. Also shown are the $F_2$ $\mu p$ scattering measurements from BCDMS.

## 2.3 Quantum Chromodynamics

QCD [38] is the theory of the strong interaction. In it, the strong force between quarks is carried by massless gauge bosons known as gluons. In rough analogy to charge in the QED case, quarks carry a strong charge-like property known as colour. There are three colour charges conventionally labelled as red, green and blue. Colour is exchanged between quarks by eight gluons which carry different combinations of colour charge. Because the gluons are coloured they interact with one another. This self interaction is in contrast to the electrically neutral, non-self-interacting photon of QED and leads to the fundamentally different character of strong interactions.

More rigorously, QCD is a non-abelian gauge theory which is invariant under the SU(3) colour transformation. The gluon self-coupling is a consequence of the non-Abelian structure of QCD.

### 2.3.1 The Strong Coupling Constant

In order to make calculations of QCD cross-sections, loop corrections to the quark-gluon coupling must be calculated. These corrections are divergent and the renormalization procedure introduces a scale into the definition of the effective coupling. This coupling depends on the scale of the QCD process, in this case defined by $Q^2$, and is said to 'run'. To leading order, the effective coupling is given by:

$$\alpha_s\left(Q^2\right) = \frac{12\pi}{(33 - 2n_f)\ln\left(Q^2/\Lambda^2_{QCD}\right)} \tag{2.9}$$

where $n_f$ is the number of active quark flavours and $\Lambda^2_{QCD}$ is a constant that must be extracted by experiment [48]. $\Lambda_{QCD}$ can be thought of as the scale at which strong interactions become strong. Taking the size of a typical hadron as this scale suggests that $\Lambda_{QCD}$ is approximately $1\,\mathrm{fm}^{-1}$ or $200\,\mathrm{MeV}$ which is close to experimental estimates. From this equation it is possible to extract two important features of QCD:

**Asymptotic-Freedom** At large values of $Q^2$, the effective coupling $\alpha_s$ is small and the quarks in the proton can be treated as nearly-free particles. In this regime cross-sections are calculable as perturbative expansions in $\alpha_s$.

**Infrared-Slavery** At low values of $Q^2$ corresponding to large distances the effective coupling $\alpha_s$ gets large and cross-sections are no longer calculable using perturbation theory. It is this aspect of QCD that explains why we do not observe free quarks, and as a further consequence, explains the observation of jets of hadrons [49]. It implies that as the distance between quarks increases so does the force between them. In a hadron this means that the quarks cannot escape their bound state. However, if a quark in a hadron is struck with sufficient vigour to knock it "out of" the hadron, then the energy contained in the colour field between the quark and the hadron remnant increases as the separation increases. When the energy contained in the field reaches a sufficient level, quark anti-quark pair production becomes possible. This process continues until the energy of the original quark is spent and the resulting quarks and anti-quarks produced form a collimated spray of

hadrons known as a jet. This strong binding of the quarks is known as infrared slavery.

### 2.3.2 QCD Factorisation

The perturbatively calculable aspects of a DIS interaction can be separated from the long-range non-perturbative aspects. As such, the proton structure function, $F_2$, can be expressed as the convolution of a function, calculable perturbatively in QCD, and the parton distribution functions.

$$F_2\left(x, Q^2\right) = \int_x^1 \mathrm{d}x' f\left(x', \mu^2\right) \sigma\left(\frac{x}{x'}, Q^2, \mu^2\right) \tag{2.10}$$

where $f(x', \mu^2)$ is the probability of finding a quark with momentum fraction $x'$ in the proton and $\sigma(\frac{x}{x'}, Q^2, \mu^2)$ is the cross-section for that quark scattering elastically off a photon with virtuality $Q^2$ [48]. This convolution represents the fact that a quark can radiate a gluon before interaction, thus lowering its effective momentum fraction from $x' \to x$. $\mu$ here represents the scale at which this gluon radiation is absorbed into the parton density function rather than the hard-scatter cross section. This choice is essentially an arbitrary one and the physical structure function $F_2$ is independent of the choice of scale, $\mu^2$. The structure function has been factorized into a hard-scatter cross section that can be calculated in perturbative QCD and a parton density function that cannot.

### 2.3.3 DGLAP

Although it is not possible to calculate parton density functions from first principles in QCD, it is possible to predict their evolution as a function of $Q^2$. This can be done using the DGLAP evolution equations [50, 51, 52]. These equations take as input the PDFs measured at a given scale and predict the evolution of the PDFs to some new scale. This is a particularly useful feature of QCD as the PDFs are independent of the hard scattering process between two partons. The consequence of this is that a PDF measured for a hadron at one experiment can be applied at a totally different one. For example, PDFs derived from *ep* data taken at HERA are usable in calculating proton-proton cross-sections at the TEVATRON or LHC.

## 2.4 Photoproduction Physics

The simple definition of a photoproduction interaction is that it is an interaction in which the virtuality of the exchanged photon, $Q^2$, is approximately zero. In this picture the electron can be viewed as a source of almost on-shell photons and it is these that interact with the proton.

The majority of photoproduction interactions are "soft" and are characterised by final-state particles of low transverse-momentum. Because of the $Q^{-4}$ dependence in the cross section, such events dominate the physics at HERA. These "soft" events, however, are not calculable in QCD. There is no hard-scale, similar to $Q^2$ in the DIS case, and thus $\alpha_s$ is large. However, in interactions involving final-states with high transverse momenta, the transverse-

momentum can be used as a hard-scale for the perturbative calculations.

### 2.4.1 Low $P_T$ Interactions

Evidence gathered at low-energy experiments shows that the photon does not interact solely as a gauge boson. Indeed, it appears as though the photon is interacting as a hadron and suggests that there is a resolvable photon structure. Such interactions are therefore referred to as resolved photon processes. One of the most important pieces of evidence concerns the energy dependence of the total $\gamma p$ cross-section as a function of the mass of the hadronic system, which rises slowly above roughly 10 GeV [53]. This is behaviour typically seen in hadron-hadron collisions. A phenomenological model has been proposed to describe this, in which the photon is allowed to fluctuate into a vector meson with the same quantum numbers, and the scatter takes place between this meson and the hadron. This is known as the Vector Meson Dominance (VDM) model [54, 55]. The VDM model gives good agreement with data taken at low energy [56] but fails to predict the outcome of high $P_T$ interactions.

### 2.4.2 High $P_T$ Interactions

Photo-production interactions involving high transverse-momentum final-states are separated into two classes. If the photon interacts directly as a whole object in the hard subprocess, the process is classified as a direct interaction. Furthermore, resolved photon processes, in which the photon

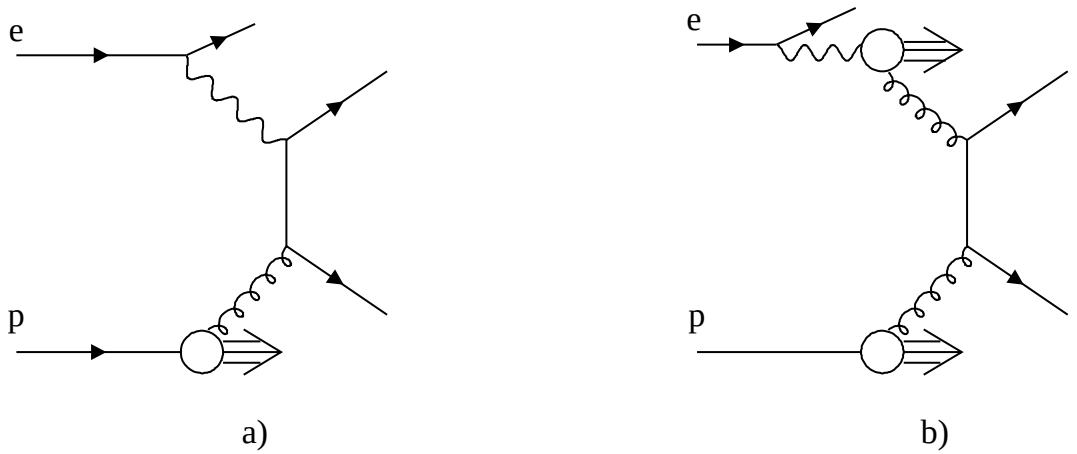


Figure 2.3: Leading-order diagrams for a) direct and b) resolved processes in photoproduction

initially splits into a $q\bar{q}$ pair without forming a bound hadronic state, are also possible. Leading-order diagrams for both direct and resolved photoproduction events are shown in Figure 2.3. These two different types of interaction give markedly different experimental topologies. In the case of direct events there is a proton remnant, indicated by the broad arrow in the lower half of Figure 2.3(a) that travels in the same direction as the initial proton, and the products of the hard subprocess. In resolved events there is also a remnant from the photon that travels in the approximate direction to the incident electron. It is indicated by the broad arrow in the upper half of Figure 2.3(b). To tackle resolved processes theoretically it is necessary to introduce the concept of parton density functions for the photon.

This direct/resolved picture is only valid at lowest order. At higher order there are ambiguities about how much of the event should be factored into the structure functions and how much into the hard subprocess [57]. As a consequence, some care must be taken in choosing variables that are well

defined at all orders. The variable $x_\gamma$ fulfils these criteria:

$$x_\gamma = \frac{\sum_{jets} (E_{jet} - p_{z,jet})}{\sum_i (E_i - p_{z,i})} \tag{2.11}$$

Here the index $i$ runs over all objects in the final-state. At lowest order, $x_\gamma$ can be thought of as the fraction of the momentum of the photon involved in the hard subprocess. For a direct process $x_\gamma$ is, by definition, one.

Inclusive N-jet photo-production in $ep$ interactions can be written as

$$e(k) + P(p) \rightarrow e(k') + jet1\left(E_T^{jet1}, \eta^{jet1}\right) + \ldots + jetN\left(E_N^{jetN}, \eta^{jetN}\right) + R \tag{2.12}$$

where $k$, $k'$ and $p$ are as defined in figure 2.1. $R$ represents the hadronic final-state not associated with the hard jets. Because the photon and proton are very nearly collinear in photo-production, a minimum of two high transverse-momentum jets is required in the final state to maintain conservation of momentum. Due to the presence of a hard scale the N-jet photo-production cross-section can be factorized, as in the DIS case, to give:

$$\frac{\mathrm{d}\sigma_{Njets}}{\mathrm{d}y} = \sum_{a,b} \int \mathrm{d}x_a \mathrm{d}x_b f_{\gamma/e}(y)\, f_{a/\gamma}(x_a)\, f_{b/P}(x_b)\, \mathrm{d}\sigma_{ab\rightarrow Njets} \tag{2.13}$$

where $f_{a/\gamma}(x_a)$ and $f_{b/P}(x_b)$ are the PDFs for partons $a$ and $b$ from the photon and proton respectively. $f_{\gamma/e}(y)\,\mathrm{d}y$, the extended Weizsacker-Williams Approximation [58, 59, 60], gives the photon flux in the fractional energy

range $y$ to $y + dy$ for photon virtualities between $Q^2_{min}$ and $Q^2_{max}$:

$$f_{\gamma/e}(y) = \frac{\alpha_{em}}{2\pi}\left[\frac{1+(1+y)^2}{y} ln\frac{Q^2_{min}}{Q^2_{max}} - \frac{2(1-y)}{y}\left(1 - \frac{Q^2_{min}}{Q^2_{max}}\right)\right] \qquad (2.14)$$

$Q^2_{min}$ is the kinematic lower limit set on $Q^2$, and $Q^2_{max}$ is the upper limit on $Q^2$ set by experimental conditions. For a direct process, $f_{a/\gamma}(x_a) = \delta(1 - x_a)$. The physics of the hard subprocess is all contained in the partonic cross-section $\mathrm{d}\sigma_{ab\to Njets}$.

## 2.5 The Top-Quark

> "The struggle to the top is, in itself, enough to fill the heart of man. One must imagine a happy Sysiphus."
>
> The Myth of Sysiphus, Albert Camus

There are now known to be at least three generations of quarks. The first generation contains the up- and down-quarks; the second the charm- and strange-quarks; and the third contains the bottom- and top-quarks. The bottom-quark was discovered in 1977 [61], but its partner resisted discovery until 1995 when the CDF and D0 experiments at FERMILAB finally measured the necessary significant effect [1, 2]. The length of this wait was due at least in part to the unexpectedly large mass of the top-quark. The mass of the top-quark is not predicted by the SM, but its value can be inferred indirectly from precision electroweak measurements [62]. The value for the mass measured in this way is in good agreement with the mass measured at FERMILAB (see Table 2.1).

| | Experiment | Theory |
|---|---|---|
| $m_t$ | $174.3 \pm 5.1\, GeV$ | $168.2^{+9.6}_{-7.4}\, GeV$ |
| $\sigma\left(p\overline{p} \rightarrow tt\right)$ | $6.2 \pm 1.7\, pb$ | $4.75 \pm 0.5\, pb$ |
| $BR\left(t \rightarrow Wb\right) / BR\left(t \rightarrow Wq\right)$ | $0.94^{+0.31}_{-0.24}$ | $\approx 1$ |

Table 2.1: Comparison of theory and experiment for top-quark physics from Run 1 of the FERMILAB TEVATRON. For discussion and references see [63, 64].

The mass of the top-quark is related to the top-quark Yukawa coupling that transmits the information that the Higgs' field has acquired a vacuum expectation value to the top-quark, thereby generating its mass. The Yukawa coupling $y_t$ to the top-quark and the mass of the top-quark are related via $y_t = \sqrt{2}m_t/v$, where $v$ is the vacuum expectation of the Higgs' field. The fact that the mass of the top-quark is close to the electro-weak symmetry-breaking scale (EWSB scale), an area of the standard model that has yet to be probed directly, suggests that the top-sector is a good place to look for new physics.

A summary of the measured properties of the top-quark are shown in Table 2.1. From this it can be seen that the top-quark decays almost exclusively to give a $W$ boson and a bottom quark. Due to the large mass of the top-quark, this decay occurs more quickly than the characteristic time-scale for hadronization [65]. Thus, studying the top-quarks allows for the unique possibility of studying the properties of the 'bare' quark, although it also denies us the rich taxonomy of hadrons that attends the other quarks. The mass of the top-quark is currently the best known of all the quark masses, although the bottom-quark is a close second [64, 3]. It is also interesting to note that, although it has not yet been directly measured, $V_{tb}$, the weak coupling between

the top-quark and the bottom-quark, is the most precisely determined of the Cabibbo-Kobayashi-Maskawa (CKM) matrix elements, which embody cross-generational mixing in the quark sector of the standard model [66]. If we assume there are only three generations of quarks, then $V_{tb} = 0.99915 \pm 0.00015$ [62]. This is due to the small measured values of $V_{ub}$ and $V_{cb}$ and the unitarity constraint $|V_{ub}|^2 + |V_{cb}|^2 + |V_{tb}|^2 = 1$. If there are more than three generations then $V_{tb}$ is known rather less well: $0.07 < V_{tb} < 0.993$ [3].

### 2.5.1 The Top-Quark at HERA

The centre of mass energy of $\sim 320\,\text{GeV}$ at HERA is below the threshold for $t\bar{t}$-quark pair production so, if top-quarks are produced at HERA, then they must be produced singly. In the Standard Model, single top-quark production is negligible in $ep$ collisions. Calculations of the charged current reaction

$$ep \to \nu\bar{t}bX$$

carried out in [4] show that at a top-quark mass of above 60 GeV the single-top production cross-section is already marginal $\sim 0.2\,\text{pb}$ and the logarithm of the cross-section falls approximately linearly with increasing top-quark mass. Neutral-current production of single top-quarks at HERA is suppressed because neutral-current reactions preserve the involved flavours at leading order. Therefore, flavour-changing neutral-current reactions only arise via higher order corrections and as such the rates are very low [67]. Because the rates for FCNC processes are so low in the Standard Model, they are an ideal place to look for physics outside the Standard Model. At HERA, interactions coupling a top-quark to a light quark (up or charm) and a gauge boson would lead to single-top production as shown in Figure

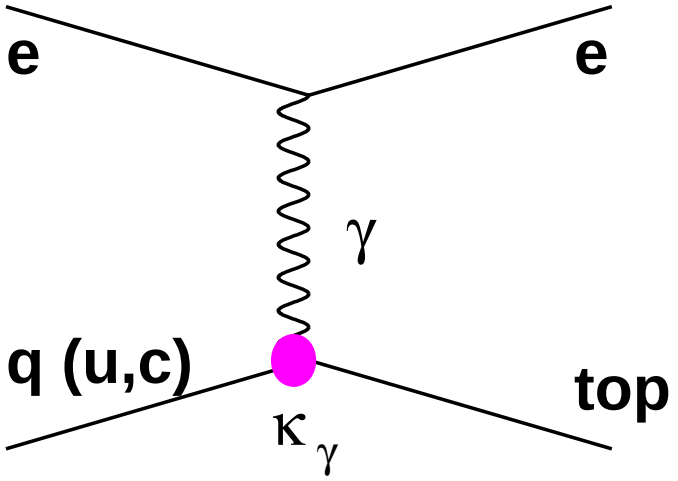


Figure 2.4: Diagram of FCNC single-top production mechanism

2.4. A general effective lagrangian, first proposed in [68], describing FCNC top-quark interactions involving electroweak bosons is:

$$\mathcal{L}_{eff} = \sum_{U=u,c} i\frac{ee_U}{\Lambda}\bar{t}\sigma_{\mu\nu}q^{\nu}\kappa_{\gamma,U}UA^{\mu} + \frac{g}{2cos\theta_W}\bar{t}\left[\gamma_{\mu}\left(v_{Z,U} - a_{Z,U}\gamma^5\right) + i\frac{1}{\Lambda}\sigma_{\mu\nu}q^{\nu}K_{Z,U}\right]UZ^{\mu} + h.c. \tag{2.15}$$

where $\sigma_{\mu\nu} = (i/2)\left[\gamma^{\mu}, \gamma^{\nu}\right]$, $\theta_W$ is the Weinberg angle, $q$ the four-momentum of the exchanged boson, $e$ and $g$ denote the gauge couplings relative to $U(1)$ and $SU(2)$ symmetries respectively; $e_U$ denotes the electric charge of up-type quarks, $A^{\mu}$ and $Z^{\mu}$, the fields of the photon and $Z$-boson, and $\Lambda$ denotes the scale up to which the effective theory is assumed to hold. The expression contains terms that represent the couplings of both $\gamma$ and $Z$-bosons to the up- and charm-quarks to give top-quarks. The strengths of these various couplings are controlled by the variables $\kappa_{\gamma,u}$, $\kappa_{\gamma,c}$, $v_{Z,u}$ and $v_{Z,c}$.

At HERA the greatest sensitivity is expected to be that to the coupling $\kappa_{\gamma,u}$. This comes from a combination of two effects. First, that the majority of interactions at HERA involve the exchange of a low virtuality (low $Q^2$)

photon. There is mixing with the $Z$-boson but this only becomes significant at high values of $Q^2$ close to the square of the mass of the $Z$-boson. The cross section goes as $\frac{1}{Q^4}$, so the sensitivity at high $Q^2$ is suppressed.

Second, that, with an incident lepton energy of 27.6 GeV, the struck quark must have a minimum momentum of 277 GeV in order to produce a single top-quark. This corresponds to an $x$ of around 0.3. At these values of $x$ the parton density of up-quarks, which appear as valence quarks, is far higher than for charm-quarks, which appear only in the quark sea.

The current best limits on these anomalous couplings come from the CDF collaboration [69]. Here limits are set on the radiative decays of top-quarks to give:

$$BR\,(t \to q\gamma) < 3.2\%\; CL\,95\%.$$

This limit constrains the coupling to be:

$$\kappa_{q\gamma} < 0.42$$

If only the couplings to photons contribute substantially to the cross-section of single-top production at HERA, the differential cross-section for the process $ep \to etX$ is given by:

$$\frac{\mathrm{d}\hat{\sigma}_\gamma}{\mathrm{d}\hat{\mathrm{t}}} = \frac{e_0^2\kappa_{q\gamma}^2}{8\pi\hat{s}^2\hat{t}}\left[\left(2\hat{s}+\hat{t}\right) - \frac{2\hat{s}\left(\hat{s}+\hat{t}\right)}{m_t^2} - m_t^2\right] \tag{2.16}$$

where $\hat{s}$ and $\hat{t}$ are the Mandelstam invariants for the process $e(p_e)+u(p_u) \to e(p_{e'})+t(p_t)$, defined as $\hat{s} = (p_e+p_u)^2$, $\hat{t} = (p_t-p_u)^2$ [70, 71]. The total cross-

section is obtained by the integral of the differential cross-section convoluted with the distribution of up-quarks in the proton:

$$\sigma_{tot} = \int_{x_{min}}^{1} f_q(x)\,\mathrm{dx} \int_{\mathrm{t_-}}^{\mathrm{t_+}} \frac{\mathrm{d}\hat{\sigma}}{\mathrm{d}\hat{\mathrm{t}}} \mathrm{d}\hat{\mathrm{t}} \tag{2.17}$$

where $t_+ = -0.002\,\mathrm{GeV}$, $t_- = -(\hat{s} - m_t^2)$, $x_{min} = m_t^2/s$ and $f(x)$ is the parameterised up-quark distribution function inside the proton, given by:

$$f_u(x) = A_u x^{\eta_1 - 1} (1-x)^{\eta_2} \left(1 + \epsilon_u \sqrt{x} + \gamma_u x\right) \tag{2.18}$$

where $A_u = 0.8884$, $\eta_1 = 0.4710$, $\eta_2 = 3.404$, $\epsilon_u = 1.628$ and $\gamma_u = 9.628$ [72].

The cross section for the process $ep \to etX$, taking into account only the coupling $\kappa_{\gamma,u}$, has been calculated in [73] and the QCD corrections which amount to a 25% increase were calculated in [71]. At a value of $\kappa_{\gamma u} = 0.15$, the predicted cross section is 0.21 pb. If the coupling $\kappa_{\gamma u}$ is allowed to saturate the upper bound set by CDF, then the expected upper limit on the cross section for single-top production at HERA is $\sim 1.6\,\mathrm{pb}$. In $104\,\mathrm{pb}^{-1}$ of data this allows for roughly 170 single-top events, which, via the branching ratios of the $W$-boson, correspond to roughly 110 hadronic top-quark decays and 20 each for the decays of the $W$-boson into the different leptonic flavours.

Alternatively, the isolated lepton events mentioned in the introduction can be used to obtain a limit on the single-top cross section. Assuming a branching ratio into electrons and muons of 22%, the result for $p_T^X > 25\,\mathrm{GeV}$ can be used to obtain an upper limit as detailed in the Appendix. Assuming an efficiency of 45% [74] for this channel, the observation of 10 events for an

expectation of $2.82 \pm 0.73$ events gives an upper limit on the single-top cross section of 1.43 pb, which although it is already tighter than the CDF limit still allows for the production of around 100 hadronically decaying single top-quarks.

It should be noted that, as the HERA centre of mass energy rose from $\sqrt{s} = 300\,\text{GeV}$ in the $1994-97$ period to $\sqrt{s} = 320\,\text{GeV}$ in the $1999-2000$ period, the expected single-top cross section rose by a factor of 1.41 [71].

# Chapter 3

# Monte Carlo Event Generators

The theoretical predictions for background and signal processes are implemented by event generators. These use fixed-order matrix-element calculations to assign probabilities for each hard subprocess. This hard subprocess is then combined with a hadronization scheme that converts the outgoing partons into observable hadrons. The factorisation theorem, mentioned in Chapter 2, implies that the two processes can be considered and calculated separately. To supplement the fixed-order matrix-element calculations some of the event generators include initial- and final-state parton showering. These parton showers simulate higher-order corrections not included in the fixed-order calculations. The hadrons generated in this way can then be fed into a complete detector simulation to give a prediction at the detector level that can be used to compare directly with the data and also to estimate the detector's effect on the data. The event generators used in this thesis and the software used to perform the detector simulation are outlined below.

## 3.1 Hadronization Models

The mechanism of hadronization, where coloured partons become colourless hadrons, is only very poorly understood. A number of models have been proposed to simulate the process. By invoking the factorisation theorem, such models aim to be applicable over a wide range of data sets without having to be tuned specifically to each.

### 3.1.1 String Fragmentation

The JETSET program implements the LUND string-fragmentation model [75]. Here, coloured partons are connected by a "string" which has an energy-density proportional to its length. As the partons are separated, the string stretches and the potential energy increases before breaking to form a $q\overline{q}$ pair. If the resulting string fragments have sufficiently high energy they can go on to form further $q\overline{q}$ pairs. The process continues until only colourless, on-shell hadrons remain, each hadron corresponding to a short length of string with a quark at one end and an antiquark at the other. This process leads to the production of mesons only. Baryons are produced by splitting the string with a diquark-antidiquark pair.

### 3.1.2 Cluster Hadronization

The cluster hadronization model used in the HERWIG event generator [76, 77] takes the outgoing gluons and splits them non-perturbatively into light quark-antiquark pairs to give a set of jets composed of quark-antiquark pairs.

After this process, quark-antiquark pairs are arranged into colourless clusters. The lighter clusters form hadrons and the heavier clusters decay to give a pair of lighter hadrons.

## 3.2 PYTHIA - Photoproduction Event Generator

The event generator PYTHIA 5.7 [78] was used for the analysis presented in this thesis to simulate photoproduction processes. Resolved and direct processes were generated separately, as were contributions from charm and bottom production. The PYTHIA generator contains the first-order QCD matrix-elements and uses leading-log parton showers and the LUND string-fragmentation model [75]. The GRV LO and GRV-G LO parton densities in the proton and photon respectively are used [79].

Events were generated over all $y$ with $Q^2 < 4\,\mathrm{GeV}$. Each of the contributions (resolved, direct, charm and bottom) was split up into two samples characterised by the transverse-momentum of the hard subprocess, $\hat{p}_T$. The first sample contains events of $\hat{p}_T > 5\,\mathrm{GeV}$ and the second contains only events with $\hat{p}_T > 17\,\mathrm{GeV}$. The second sample was generated with a much larger luminosity. Using these two samples, a large statistical sample containing the highest $\hat{p}_T$ jets that are of interest in this analysis was obtained. In total 1.15 million PYTHIA events were generated. Of these 250000 were generated for $\hat{p}_T > 17\,\mathrm{GeV}$ and the remainder were generated for $\hat{p}_T > 5\,\mathrm{GeV}$.

## 3.3 HERWIG - Photoproduction Event Generator

The hard subprocess in HERWIG is similar to that in PYTHIA. However, HERWIG includes a complete coherent showering algorithm that is applied to initial- and final-state radiation [76, 77].

HERWIG events were generated over the same kinematic range as the PYTHIA sample, with $\hat{p}_T > 6\,\text{GeV}$ and $\hat{p}_T > 17\,\text{GeV}$ samples being created. The cluster-fragmentation model is used by HERWIG to hadronize the outgoing partons. HERWIG is used in this analysis to cross-check the photoproduction rates from PYTHIA.

## 3.4 RAPGAP - DIS Event Generator

To model the background contribution coming from Neutral-Current events the RAPGAP generator was used [80]. 830000 NC DIS events with $Q^2 > 4\,\text{GeV}$ were generated using RAPGAP 2.8, which utilises leading-order matrix elements, with the CTEQ4M parameterizations for the proton [72]. The photon is assumed to be structureless in the DIS case. QED radiation from the initial- and final-state electron are simulated with the HERACLES program [81]. Hadronization was simulated using the LUND fragmentation model. Together with events generated using PYTHIA these two programs cover the whole range in $Q^2$.

## 3.5 EPVEC - Heavy Particle Decay Event Generator

The EPVEC generator takes an electron and a proton as the initial-state particles and produces vector bosons. It is a set of FORTRAN functions based on [82] that simulate the parton-level processes for vector-boson production not included in the PYTHIA generator. The generator used here is the H1EPVEC generator [83] that implements EPVEC within the H1 computing environment using the PYTHIA [78] framework. 100000 events were generated.

## 3.6 ANOTOP - Anomalous Single-Top Event Generator

The simulation of the single-top signal relies on a specific event generator ANOTOP using the matrix elements of the complete $e+q \rightarrow e+t \rightarrow e+b+W \rightarrow e+b+f+\overline{f'}$ process as obtained from the CompHEP program [84]. This allows a proper description of angular distributions. The BASES/SPRING package [85] is used to perform the numerical integration of the amplitudes and to generate events according to the differential cross-section. The parton-showers approach, relying on the DGLAP evolution equations [51, 50, 52], is used to simulate QCD corrections in the initial- and final-states. The parton densities used [72] are evaluated at the scale of the mass of the top-quark. In total, 50000 single-top events were generated.

## 3.7 Predictions of QCD-based Models after Detector Smearing

A comparison of the predictions of the QCD-based Monte Carlo models with uncorrected data is made using the H1SIM detector simulation. This makes use of the GEANT software package [86, 87]. The parameters used in this program were determined in test-beam measurements and optimised during *ep* data taking. To save computing time the energy response of the calorimeters is simulated using a fast parameterisation for the development of electromagnetic and hadronic showers as implemented in H1FAST [88, 89]. These simulated events are subject to the same reconstruction program as the data, and also the same analysis chain.

# Chapter 4

# Jet Algorithms

Due to the nature of interactions in QCD, and particularly the self-interaction of the gluons, the energy contained in the colour field between two separated quarks increases with increasing separation. In one phenomenological model - the one used in the analysis presented in this thesis [75] - if the quark separation increases, then, at a particular point, the energy contained in the field exceeds that needed to produce a quark-antiquark pair from the vacuum. This process will repeat until the kinetic energy of the quarks is dissipated and the quarks have grouped off to form hadrons. From conservation of momentum, these hadrons will tend to be travelling in the same direction as the initial quarks that produced them. Because the transverse-momentum of the hadrons relative to this direction will be small by comparison to the longitudinal component, these sprays of hadrons are observed as collimated jets.

Because the hadrons are associated with the fields between the partons and

not directly with the partons themselves, there is no precise one-to-one correspondence between partons involved in the hard scattering process and the jets they produce. This means that there is no unique assignment of particles to a jet and, as such, jets are a matter of definition. However, there are a number of properties that are desirable in a jet algorithm.

The definition should be applicable in both the theoretical and experimental cases. In the theoretical case it is also desirable if the definition is valid at all stages of the simulation, from the hard-scatter partons, through hadronization and showering, to the full detector-level simulation. In addition, and despite the fact that there is no unique one-to-one identification between the hard-scatter partons and jets, it is helpful intuitively if there is a close correlation between the two.

## 4.1 Infra-red and Collinear safety

There are two further points that need to be addressed, both of which stem from divergences in the perturbative expansion for the partonic cross-section [90]. These occur when either there are two massless parallel partons in the final-state (collinear divergence), or when there is a parton produced with a vanishingly small energy (infra-red divergence). In the total cross-section calculation these divergences are cancelled by virtual contributions. In the jet case they are avoided by treating two parallel partons as a single parton with a momentum equal to the sum of the two, and by the requirement that the jet algorithm is insensitive to the addition of soft partons. Similar problems

are manifest in the experimental case. Two almost parallel particles will be measured either in the same calorimetric cell, or in neighbouring cells, and this distinction should not affect the final choice of the jets. The infra-red problem has an analogue in that the jet-finding should be unaffected by the presence of low-energy calorimetric noise.

## 4.2 Jet Algorithms

The information obtained from the calorimeters, trackers and other systems is combined to give a list of objects associated with particles propagating through the H1 detector. In the experimental case a jet algorithm takes as input a list of these objects, their energy and momenta. Some of these objects are composite, using both the track and calorimetric information to give the best possible knowledge of the particles momenta. A jet algorithm works by recombining these objects, generally by some iterative process, into compound entities that are jets by the definition of the algorithm. The algorithm is the definition of a jet.

The objects used by the jet algorithm need not be the actual measured particles. The algorithm should work on objects produced at all stages of event simulation. These include: the outgoing partons from the hard scatter process; particles produced in the hadronization process; and fully simulated objects at the detector level.

## 4.3 Recombination Schemes

There are a number of methods by which the particles can be recombined. The method used in the jet algorithm used in this analysis is the $E_T$-weighted recombination scheme. In this scheme the jets are taken as massless and the jet variables are formed in the following way:

$$E_{T_{jet}} = \sum_i E_{T_i}, \quad \eta_{jet} = \frac{\sum E_{T_i}\eta_i}{\sum E_{T_i}}, \quad \phi_{jet} = \frac{\sum E_{T_i}\phi_i}{\sum E_{T_i}} \tag{4.1}$$

Because the jets are massless, the energy and momentum of the jet are the same and the rapidity is equivalent to the pseudo-rapidity.

## 4.4 Inclusive $k_T$ Algorithm

In a clustering algorithm, pairs of objects are recombined one at a time. The pair that is combined at any particular iteration consists of the two objects that fall closest together in some parameter space. It is the choice of this parameter that differentiates between the different types of clustering algorithm. One of the first such algorithms, proposed by the JADE collaboration [91], used the invariant mass of pairs of objects as a closeness parameter. This however leads to widely separated, low-energy particle pairs being combined, which goes against the intuitive idea that we have of a jet. To get around this problem, the $k_T$ family of clustering algorithms was proposed [92], in which the parameter used to judge closeness is the relative transverse momentum of the softer particle of a pair to the harder. The longitudinally invariant $k_T$

algorithm (implemented using the KTCLUS [93] package) belongs to the $k_T$ family of algorithms. Its implementation is outlined below:

1. The algorithm starts with a list of all particles and an empty list of jets.

2. A distance $d_{ij}$ is calculated for every pair of particles and $d_i$ for each particle, according to

$$d_i = E_{T,i}^2 R_0^2 \tag{4.2}$$

$$d_{ij} = min(E_{T,i}^2, E_{T,j}^2) R_{ij}^2 \tag{4.3}$$

$$R_{ij}^2 = \Delta\eta_{ij}^2 + \Delta\phi_{ij}^2 \tag{4.4}$$

3. $d_{min}$ is defined as the smallest value of all $d_i$ and $d_{ij}$.

4. If $d_{min}$ belongs to the set of $d_{ij}$, the recombination procedure outlined in section 5.2 is used to merge particles $i$ and $j$ into a new 'pseudoparticle', and $i$ and $j$ are removed from the particle list.

5. If $d_{min}$ belongs to the set of $d_i$, the particle $i$ is removed from the list of particles and added to the list of jets.

6. The procedure is finished when the list of particles is exhausted. At this stage all particles are assigned to single jets.

This jet definition implies that particles with $R_{ij} < R_0$ are subsequently merged, so that all final jets are separated by distances $R_{ij} > R_0$. The parameter $R_0$ is the distance scale between particles, regardless of the jet

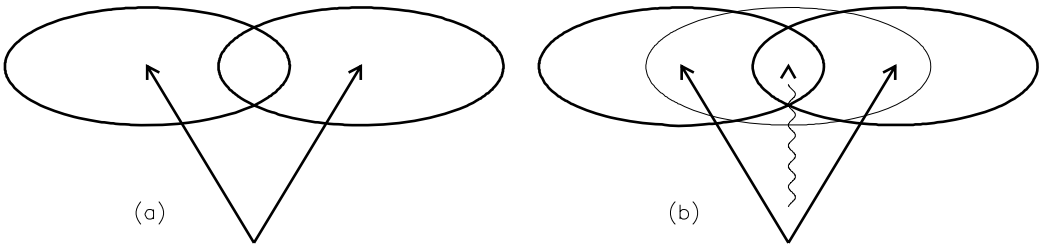


Figure 4.1: Schematic representation of the infra-red danger posed by careless use of the cone algorithm. In (a) the two jets are separated by a distance $> R_0$. The introduction of a soft parton in (b) creates a new cone that contains the original jet pair.

axis. $R_0$ is typically set to 1 as this choice treats initial- and final- state radiation equally.

## 4.5 The Cone Algorithm

In cone algorithms, jets are found by allowing their axes to vary such that the energy flow is maximised in a cone of radius $R_0$, in pseudo-rapidity and azimuth space, around that axis. Despite the appealingly intuitive idea, cone algorithms run into difficulties when faced with overlapping jets. When jets overlap, the introduction of soft-particles can have a large effect on the jet properties, which violates the requirement, mentioned above, of infra-red safety [94]. Figure 4.1 shows how this can arise in a simple situation. In Figure 4.1 (a) the two particles, separated by a distance greater than $R_0$, form two distinct jets. In Figure 4.1 (b) however, the addition of a soft particle between the two jets can cause them to be recombined into a single jet. This difficulty can be avoided by taking the mid-point of all jet pairs as the seed for the jet-finding. In this way the hard jets in Figure 4.1 would

form a single jet regardless of the soft particle introduced between them. A cone algorithm that does this is detailed below.

1. Each particle in the event is considered as the seed of a jet, for which steps 2 to 4 are performed.

2. The jet momentum is calculated for all particles within a radius $R_0$ around the seed direction, according to the recombination scheme detailed in 4.1.

3. If the jet direction differs from the seed direction then the jet direction is taken as the new seed direction and step 2 is repeated.

4. If the jet direction and seed direction coincide then a stable jet direction has been achieved and the jet is stored in a list of protojets. Two directions are said to coincide if the cones around each one contain the same objects.

5. To ensure the infra-red safety of this procedure, steps 2 to 4 are repeated with the midpoints of all pairs of protojets as seed directions.

6. Protojets with transverse energies $E_{protojet} < \epsilon$ are removed from the list of protojets.

7. The protojets that share more than a fraction $f$ of their transverse energy with a protojet of higher transverse energy are also removed from the list.

8. All particles that are contained in more than one protojet are assigned to the protojet whose axis is closest in $\eta, \phi$ space. The jet momenta are then recalculated according to the prescription detailed in Section 4.3.

9. Finally all protojets with $E_{protojet} < \epsilon$ are deleted and the remaining protojets are elevated to the status of jets.

Typically $\epsilon = 5\,\mathrm{GeV}$ and $f = 0.75$. The reassignment of particles to jets and the recalculation of jet axes may result in particles being assigned to a jet of which the axis is a distance greater than $R_0$ from them. $R_0$ was set to 0.7.

The cone algorithm is not used in the main analysis in this thesis. However a variant on it is used in the triggering described in section 5.2 where a fast, infra-red dangerous cone algorithm is used to combine calorimetric clusters into jets.

# Chapter 5

# Event Selection

The work presented in this thesis is a search for evidence of the production of single top-quarks which then decay via the hadronic channel. In this channel, the top-quark decays to a bottom-quark and a $W$-boson. The $W$-boson then decays to give a quark pair. The resulting signal is an event containing three, or more, jets from the hadronization of the quarks. The main background to this signal comes from multi-jet DIS and $\gamma p$ events.

To separate single-top events from other multi-jet events, other features of top-quark decays are used. The $p_T$ spectra for jets in DIS and $\gamma p$ events fall exponentially. In single-top events the three jets are expected to have high transverse momentum owing to the large mass of the top-quark. Therefore, selecting events that contain high $p_T$ jets removes a large proportion of the background while minimizing the number of single-top events that are removed.

Another useful variable is the invariant mass of the jets in the event. For

single-top production this variable peaks around the mass of the top-quark, but for DIS and $\gamma p$ events the spectrum of invariant mass is again steeply falling. Further use can also be made of the fact that two of the jets in single-top production come from the decay of a real $W$-boson. Additional angular relationships between the decay products of the top quark can also be exploited to improve the signal to background ratio. The detailed selections made are described below.

In all that follows, the top efficiency is defined as the percentage of simulated hadronic decays of single-top events that survive all cuts applied at that point. It does not take into account the different decay channels of the top-quark. Since the branching fraction for the decay of a $W$-boson into a quark pair is two thirds, the percentage of *all* single-top decays surviving the cuts is two thirds times the top efficiency as defined here.

## 5.1 Data Sets

Between 1994 and 1997 the HERA accelerator made collisions in the H1 detector using positrons and protons at an energy of 27.5 GeV and 820 GeV respectively to give a centre of mass energy, $\sqrt{s} = 300\,\text{GeV}$. Between 1999 and 2000 the HERA accelerator made collisions again with positrons at an energy of 27.5 GeV but with a protons at an energy of 920 GeV to give a higher centre of mass energy, $\sqrt{s} = 318\,\text{GeV}$. Data taken under normal running conditions in these periods were used in the analysis presented here. Between 1994 and 1997 the H1 experiment gathered $35.6\,\text{pb}^{-1}$ of data. In

the period 1999 to 2000 the H1 experiment gathered $68.5\,\mathrm{pb}^{-1}$ of data [14].

## 5.2 Selection of Multi-jet Events

When events pass from L4 of the trigger they are assigned to a class which is based on the coarse topology and kinematics of the event. The first selection made selects events containing jet topologies and/or high transverse energy. The relevant event classes for this analysis are 5, 7 and 11 and are defined as follows:

- Class 5 contains events with high total transverse energy. It has a requirement that the total transverse energy measured in the Liquid Argon Calorimeter is greater than 50 GeV.
- Class 7 contains events with jets of high transverse energy. It has a requirement that there is a jet in the event with a transverse energy greater than 10 GeV and a $z$-vertex from the CJC that satisfies $-60\,\mathrm{cm} < \mathrm{zvtx}_{\mathrm{CJC}} < 110\,\mathrm{cm}$.
- Class 11 contains events with multiple jets. It requires two jets with transverse energies greater than 6 GeV and 10 GeV, a jet pair with invariant mass greater than 70 GeV, or a forward jet with transverse energy greater than 5 GeV.

In the Class definitions, jets are found using a simple cone algorithm. Although the algorithm is not infra-red safe, it can be used here safely, as the final selection picks events with far higher transverse energies.

## 5.3 Subtriggers

The H1 trigger system is not perfectly efficient. A small fraction of $ep$ events are rejected as well as non-$ep$ backgrounds. To determine how significant this inefficiency is, the efficiencies of the subtriggers used are calculated. The subtriggers used in this analysis, s64, s66, s67, s75, s76 and s77 are based on LAC trigger elements and have additional timing and vertex requirements.

The efficiency is found by selecting events using a monitor trigger and looking at the fraction of these events that also fire one of the analysis subtriggers. The monitor subtrigger must have no conditions in common with the analysis subtriggers, but still select events that pass the analysis cuts. The monitor subtrigger chosen here is the $s0$ subtrigger that requires energy deposited in the SPACAL. The subtrigger efficiency is defined as:

$$\epsilon_{subtrigger} = \frac{N(monitor\, subtrigger\, AND\, analysis\, subtrigger\, fired)}{N(monitor\, subtrigger\, fired)}$$

where $N(x)$ is the number of events fulfilling condition $x$. The trigger efficiencies are shown as a function of the transverse-momentum of the leading jet in Figure 5.1. The efficiency of the combined subtriggers as a function of the transverse momentum of the leading jet is shown in Figure 5.1. It can be seen that as the transverse-momentum of the jet rises above 25 GeV, the value at which it is cut in the analysis, the trigger efficiency rises above 95%. The rise of efficiency from low jet $p_T$ is due to the thresholds in the LAC requirements of the triggers. In order to check that the choice of monitor subtrigger does not introduce a bias in the efficiency, the trigger efficiencies

were calculated using simulated events. The simulation was found to be in good agreement with the trigger efficiencies in the data. Additionally the efficiency was calculated for events that fulfilled one or more of the analysis subtriggers and passed the high transverse-momentum jet selection cuts that are described in Section 5.5. The efficiency was found to be 100%. The L4 selection was also 100% efficient.

## 5.4 Reconstruction of the Hadronic Final-State

Following this initial selection, the event is fully reconstructed. The hadronic final-state must be reconstructed in a way that most closely describes the event structure before detector smearing. It is not possible to do this from data alone. Monte-Carlo simulations of the detector response and the underlying physics processes of the *ep* scattering are needed to correct the data for these effects. These are discussed in Chapter 3.

A software package known as The Hadronic Final-State (HFS) [95] takes the event vertex, calorimeter clusters, and tracks, and builds up the best hypothesis for the hadronic final-state. The package takes account of calorimeter calibration, noise reduction, track selection and cluster/track combination. Although the sole use of calorimetric information is well suited to jet studies, the inclusion of tracker information can improve energy resolution. The momenta of low-energy charged particles, manifested as curved tracks in the drift chambers, are poorly measured in the calorimeters due to the $\frac{1}{\sqrt{E}}$ dependence in their resolution. The low radius of curvature in the track-

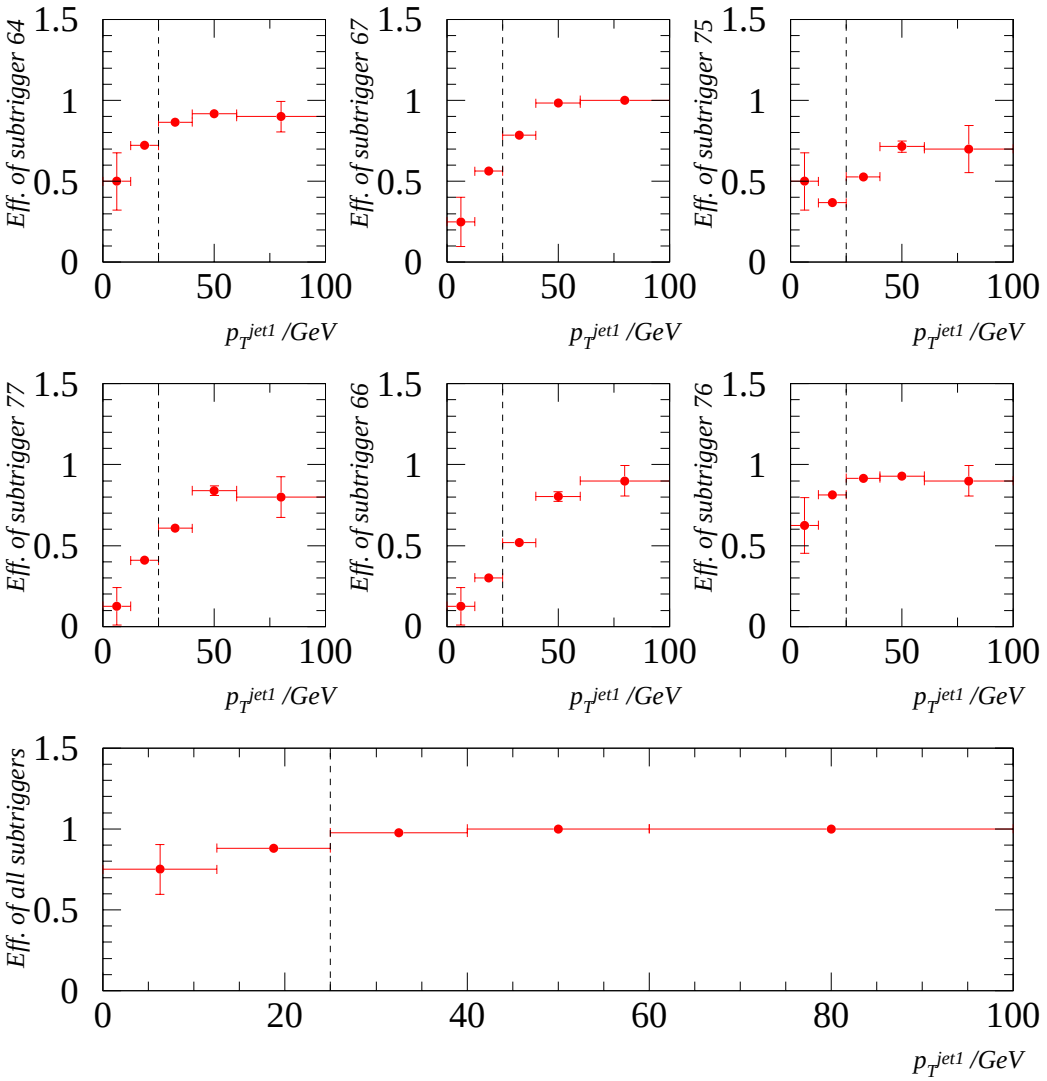


Figure 5.1: The total subtrigger efficiency for each subtrigger used in this thesis, and the combined efficiency of all six subtriggers, binned in leading jet $p_T$. The dashed lines represents the cuts made on the leading jet $p_T$.

ers, however, allows for a much more accurate measurement. 'Good' central tracks with small transverse momenta $< 2\,\text{GeV}$ are selected and extrapolated to the calorimeter surface. Energy in the calorimeter within a cylinder of radius 20 cm around the track-impact point is assigned to the track. If the calorimetric energy in this cylinder exceeds the track momentum the calorimetric energy is used. Otherwise the track momentum is taken and the calorimetric energy is neglected. If a track does not reach the calorimeter, the track momentum is also used. If the momentum of the particle is greater than 2 GeV then the calorimetric information is used. In this way the algorithm combines the track and cluster information and avoids double counting of energies. At this stage muon candidates are also selected. Energy in the calorimeter behind hits in the muon detectors is masked before jet finding to avoid double counting of energies.

### 5.4.1 Jet-Finding and Calibration

Once the hadronic final-state has been reconstructed, the objects are then used as the basis for jet-finding. As discussed in Chapter 4, the algorithm used in this analysis was the inclusive $k_T$ algorithm.

Because it is impossible for the entire mass of the detector to actively participate in detection, any particle traversing it must necessarily lose energy via interactions with dead material. This energy-loss can be calculated via Monte Carlo-based simulations [96] by comparing the jet transverse-momenta at hadron level (before detector simulation) and at detector level (after detector simulation). The energy-loss is typically below 5% and arises from

particle interactions with passive material in front of the calorimeter and energy flow into uninstrumented "cracks" within the substructure of the LAC. A variation in energy-loss is seen as a function of the impact point of the jet on the calorimeter in the $z$-direction and there is no significant variation with jet $p_T$.

The transverse-momentum of each jet in the data and the simulation is rescaled as a function of position of the $z$-impact of the jet on the calorimeter using a polynomial function derived from Monte-Carlo based simulations. Figure 5.2 shows the reconstructed top-quark mass before and after the jet calibrations are applied. After calibration, the peak in invariant mass has shifted to the top-quark mass of $\sim 174\,\text{GeV}$ that was input to the generator.

## 5.5 High Transverse-Momentum Jet Selection

After the preselection and reconstruction of the events, a high-$p_T$ 3-jet selection is made according to the following cuts.

- $-35\,\text{cm} < \text{zvtx} < 35\,\text{cm}$. Events are selected with a vertex $zvtx$ within 35 cm of the nominal interaction vertex in the $z$ direction. This has the dual effect of removing background arising from non-$ep$ physics and also ensuring that the events are well reconstructed.
- $n_{jets} \geq 3$. Events are required to contain three or more jets.
- $p_{T_{jet\,1}} \geq 25\,\text{GeV}$, $p_{T_{jet\,2}} \geq 15\,\text{GeV}$ and $p_{T_{jet\,3}} \geq 10\,\text{GeV}$, where $p_{T_{jet\,n}}$

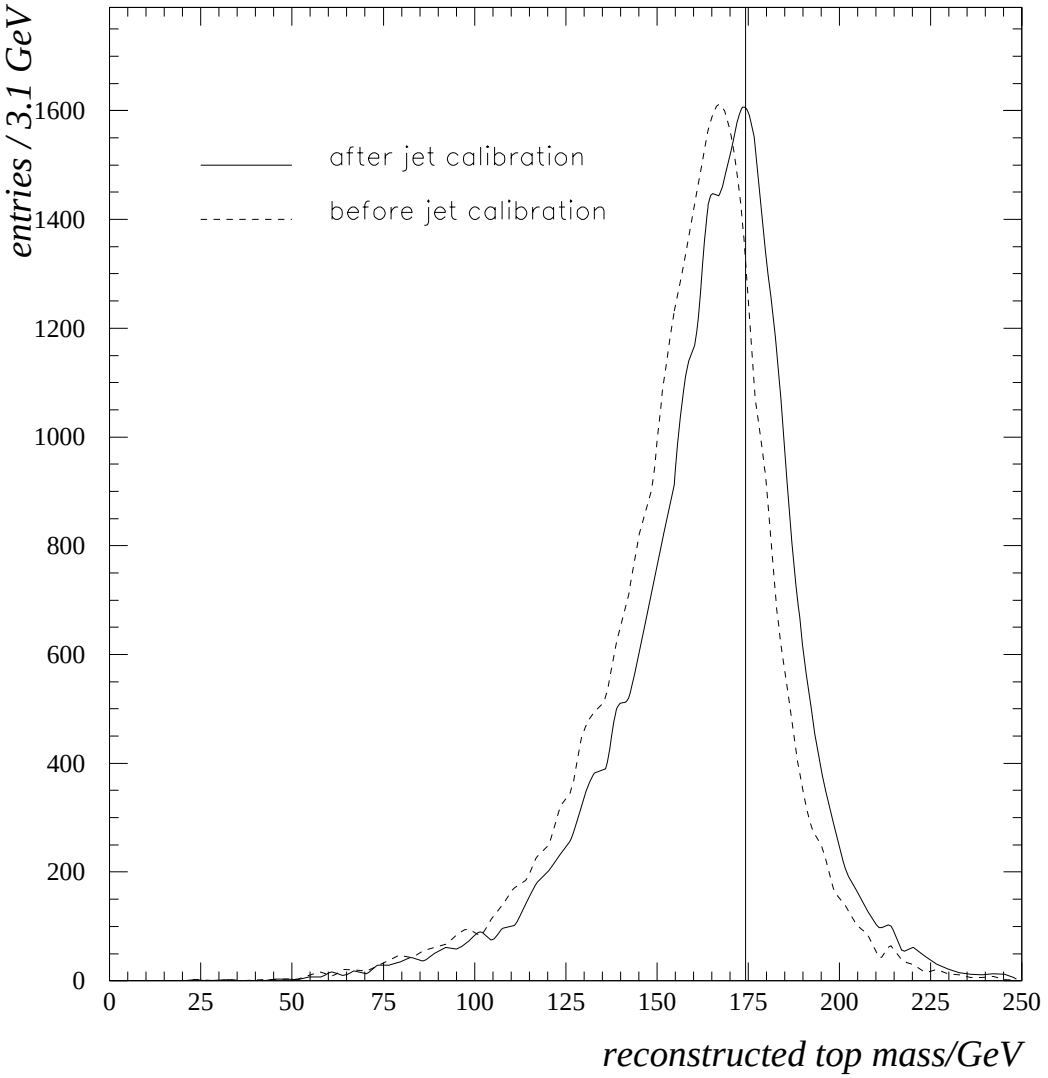


Figure 5.2: Distribution of reconstructed top-quark mass calculated by taking the invariant mass of all jets in events generated using the ANOTOP event generator. The dotted line shows the distribution before jet calibrations are applied and the solid line shows the distribution after the calibrations were applied.

is the transverse-momentum of the $n^{th}$ jet; the jets are ordered in descending $p_T$. The selection ensures that a hard scale is present in the event. The asymmetric cuts on the transverse momenta ensure that future next to leading order QCD calculation can be made with the data [97].

- $-0.5 < \eta_{jet_{1,2,3}} < 2.5$. The three high-$p_T$ jets are required to fall in a range of pseudo-rapidity which ensures that the jets are well contained in the LAC.

- $y_{jb} < 1.2$. Here, $y_{jb}$ is calculated according to $y_{jb} = \frac{1}{2E_e}\sum_i (E_i - p_{z_i})$, where the index $i$ runs over all the particles detected in the event. This removes non-$ep$ events for which $y_{jb}$ should lie between 0 and 1.

The cuts on the transverse momenta of the three leading jets are asymmetric to ensure stability of the jet cross sections at next-to-leading order [97].

After this preselection the top efficiency is 55%. This inefficiency is due mainly to the angular cuts that ensure the jets are fully contained in the LAC and thus well measured.

## 5.6 Distributions of the Final-State

Following the selection outlined above, distributions of hadronic final state observables in H1 data are shown in Figures 5.3, 5.4, 5.5 and 5.6. The predictions of QCD-based models, PYTHIA for photoproduction and RAPGAP for DIS, are also shown. It was found that, in order to obtain a satisfactory

description of the data the photoproduction contribution had to be scaled upwards by a factor of 1.19. This model deficiency has been reported elsewhere [96] and is not surprising in view of the limitations of the leading order QCD prescription used here and uncertainties in the partonic structure of the photon.

In each plot the data events that pass the 3-jet high-$p_T$ jet selection are shown as red points with associated error bars. The solid black histograms represent all contributions to the simulated background. The dotted green histograms represent the contribution to the background purely from the DIS event generator RAPGAP. The shaded yellow region indicates the combined systematic and statistical errors on the background which are described later in Chapter 6.

### 5.6.1 Figure 5.3

Figure 5.3(a) shows the distribution of the scalar transverse energy $\sum E_T$. Here, $\sum E_T$ is the scalar sum of the transverse energies of all particles in the event. The distributions fall rapidly. The distributions of the leading-jet transverse momenta $p_{T_{jet-1}}$, $p_{T_{jet-2}}$ and $p_{T_{jet-3}}$ are shown in Figures 5.3(b), (c) and (d) and also fall steeply. The predictions of the QCD-based models describe the data reasonably well, although there is a suggestive, but not significant excess at large transverse momenta.

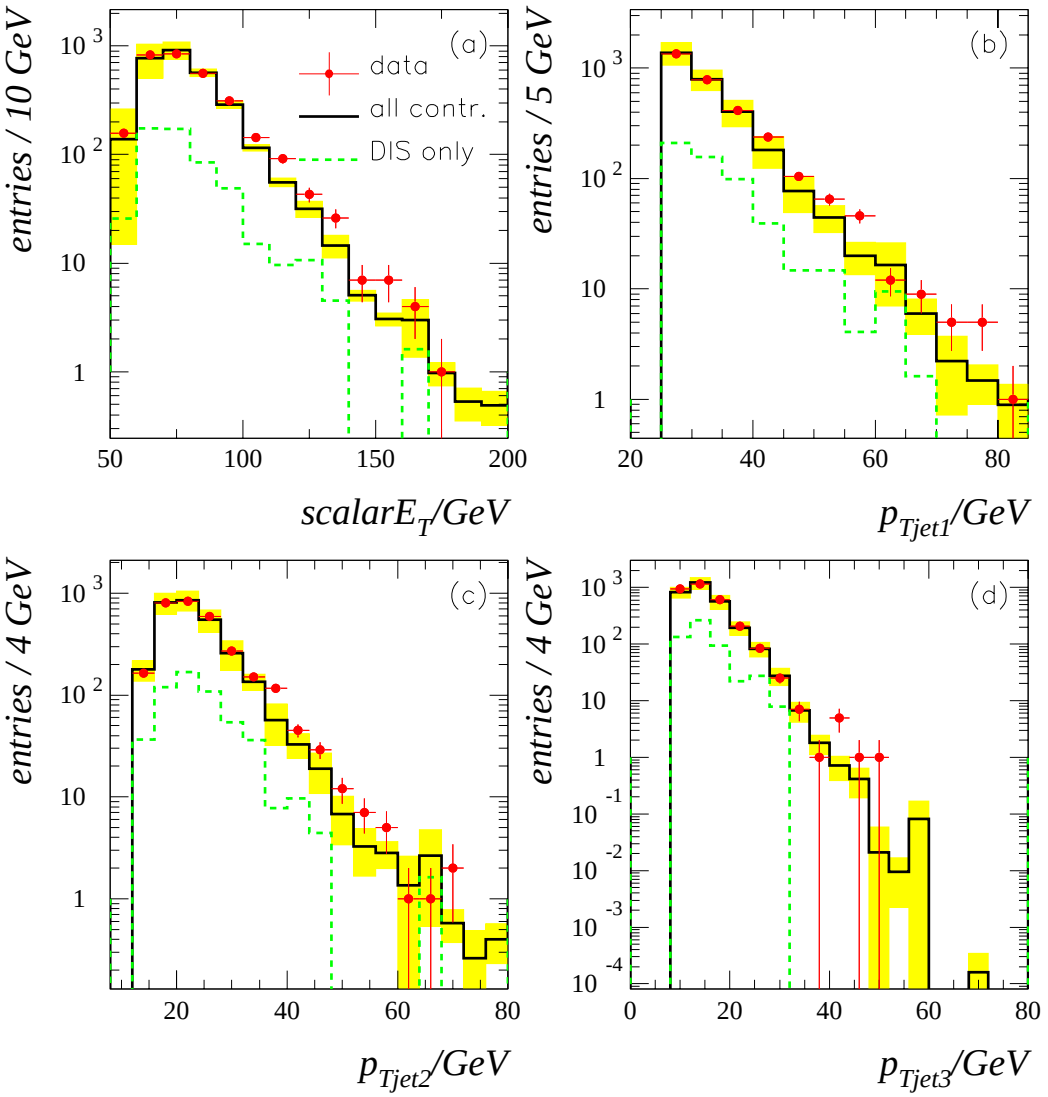


Figure 5.3: Distributions of $\sum E_T$, $p_{T_{jet\,1}}$, $p_{T_{jet\,2}}$ and $p_{T_{jet\,3}}$ as defined in the text. In each diagram, the red points represent the data and the black solid histogram and yellow shaded area represent the simulated background and its error. The green dotted histogram represents the DIS contribution to the background.

### 5.6.2 Figure 5.4

Figures 5.4(a), (b), (c) and (d) show the distributions of $M_{tot}$, $M_{12}$, $M_{13}$ and $M_{23}$ respectively. $M_{tot}$ is the invariant mass of all the jets in the event that pass the $\eta_{jet}$ cuts. $M_{ij}$ represents the invariant mass of the combined $i^{th}$ and $j^{th}$ jets. The distributions are seen to peak and fall off towards higher values of mass. The behaviour of the data is again described reasonably by the simulation. And again there is suggestive but not significant excess at high invariant masses.

### 5.6.3 Figure 5.5

Figures 5.5(a), (b), (c) and (d) show the distributions of $p_{T_{miss}}$, $n_{jets}$, $x_\gamma$ and $zvtx$ respectively. Here, $p_{T_{miss}}$ is the missing transverse-momentum as measured in the LAr calorimeter and is seen to peak around 2 GeV and fall quickly. Neutral-Current $ep$ events with a tagged electron should be balanced in transverse-momentum. Neutral-current events lacking an identified electron, charged-current events, and various non-$ep$ backgrounds, however, could contribute at high $p_{T_{miss}}$. This variable is well described by the simulation. The distribution of $n_{jets}$, i.e. the number of jets in the events that pass the $\eta_{jet}$ cuts, falls steeply since an extra order in $\alpha_s$ is required to produce each additional jet in the cross-section calculation, thus suppressing the spectrum. The variable $x_\gamma$, defined in equation 2.11, can be considered to be the fraction of the momentum of the photon that is involved in the hard subprocess. High-$p_T$ events like those considered here require a large subprocess centre of mass energy and therefore $x_\gamma$ peaks towards one. The

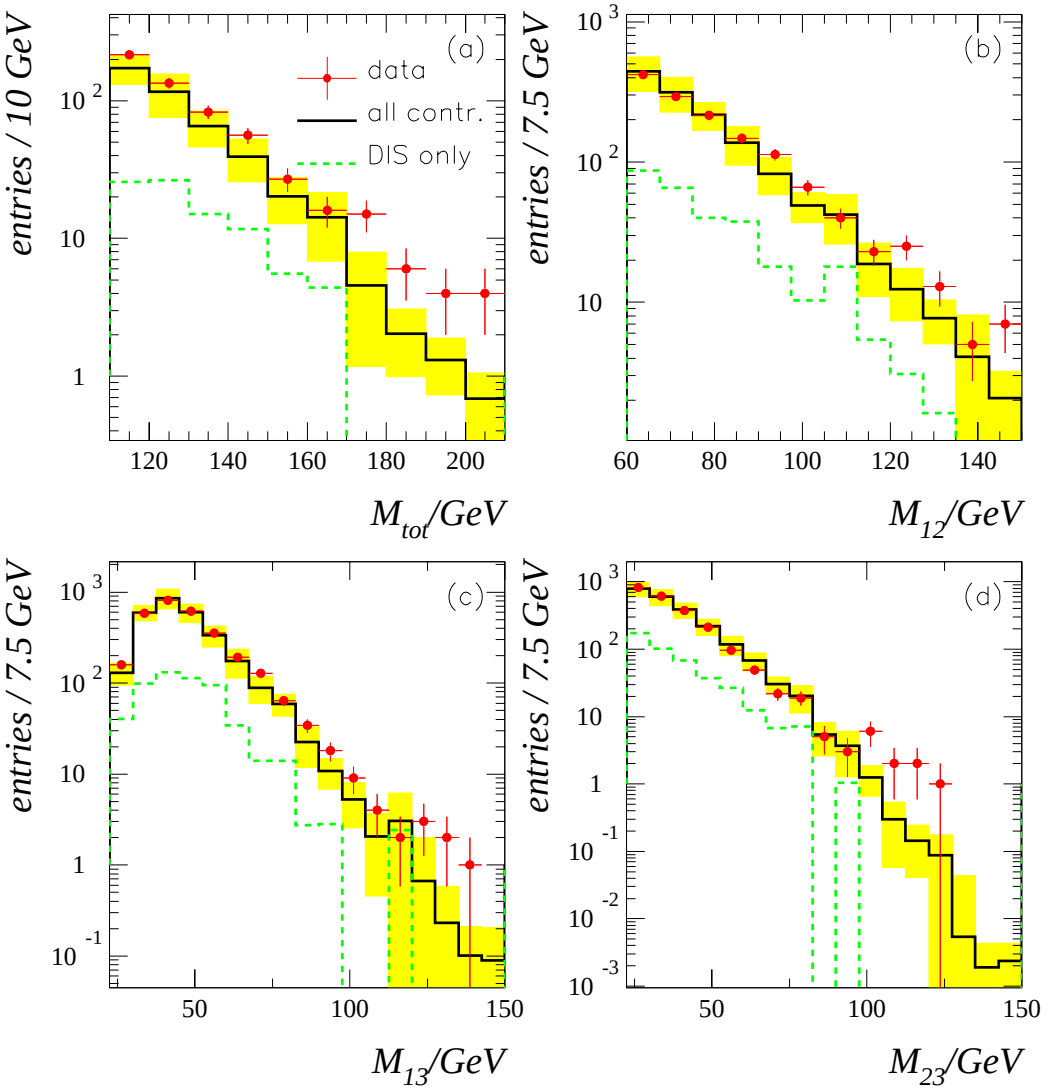


Figure 5.4: Distributions of $M_{tot}$, $M_{12}$, $M_{13}$ and $M_{23}$ as defined in the text. In each diagram, the red points represent the data and the black solid histogram and yellow shaded area represent the simulated background and its error. The green dotted histogram represents the DIS contribution to the background.

QCD-based models fail to describe the high $x_\gamma$ region and this could be due to the absence of higher-order corrections in the simulation [96, 98, 99]. The distribution of the reconstructed $z$ vertex of the event peaks near zero and has a width of about 10 cm as expected for a sample dominated by $ep$ collisions. The Monte Carlo generated events from the QCD-based models were reweighted to the $zvtx$ distribution of the data in order to reproduce the data well.

### 5.6.4 Figures 5.6

Figures 5.6(a) and (b) show the distributions of the energy and polar angle of the scattered electron, $E_e$ and $\theta_e$, respectively. Figures 5.6(c) and (d) show the virtuality of the exchanged photon, and $y$ the inelasticity of the event, respectively, as calculated from the scattered electron. The distributions are plotted for a sub-sample of the 3-jet sample for which an electron with a good-quality track and an energy of greater than 10 GeV is required. Electrons are identified as tracks that point towards well-contained energy deposits with a centre of gravity in the electromagnetic portion of the calorimeter. This identification is handled by the QESCAT electron finder [100]. The longitudinal momentum balance, $\sum_i (E_i - p_{z_i})$, where the sum runs over all objects in the final-state, is constrained to lie between $40 < \sum(E - p_z) < 65$ [26]. The $p_T$ − balance of the event, the ratio $p_{T_{hadrons}}/p_{T_{electrons}}$, is constrained to be less than 2. After this selection, a well-measured neutral-current sample with an identified electron is obtained that contains a minimum of contamination from events in which the scattered electron is not identified.

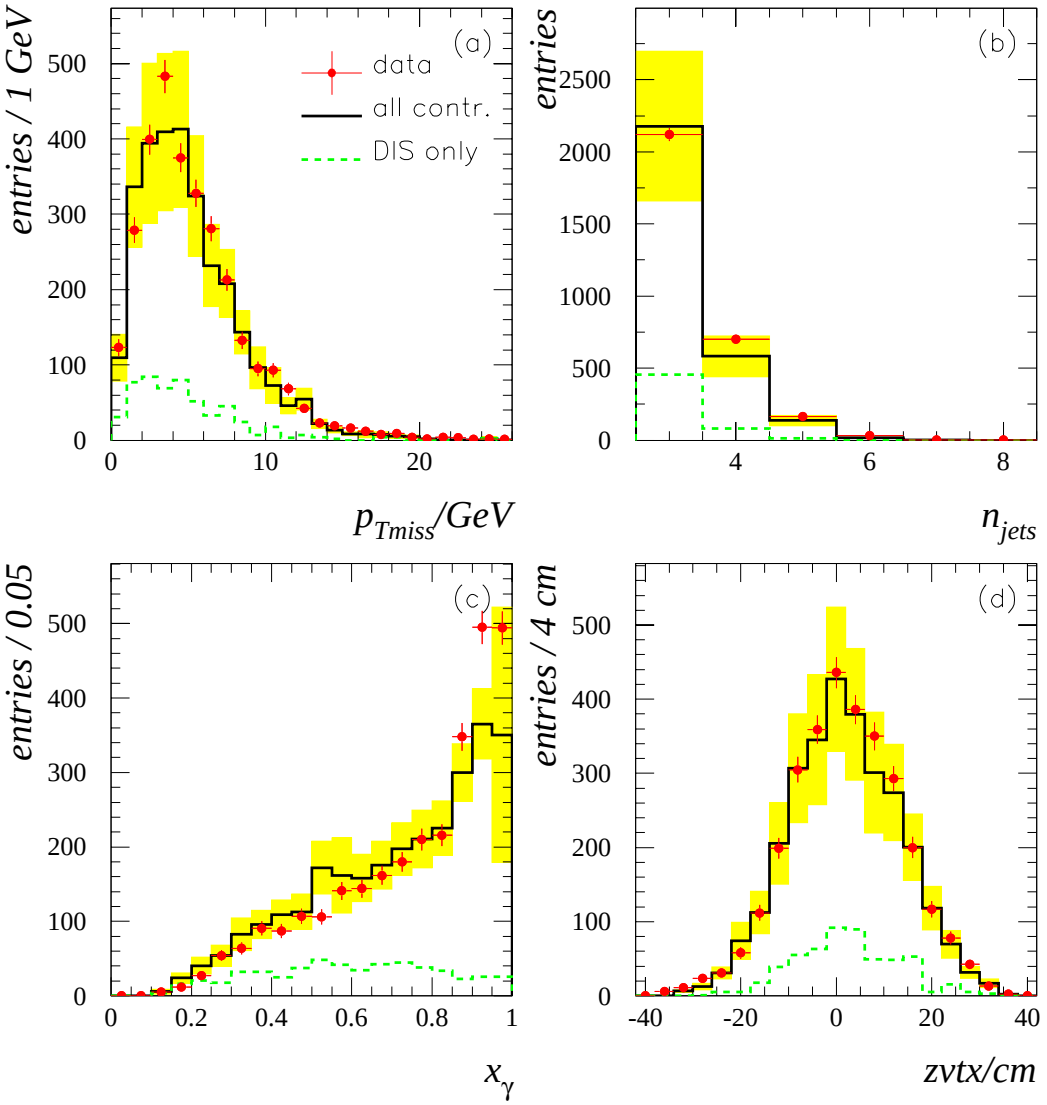


Figure 5.5: Distributions of $p_{T_{miss}}$, $n_{jets}$, $x_\gamma$ and $zvtx$ as defined in the text. In each diagram, the red points represent the data and the black solid histogram and yellow shaded area represent the simulated background and its error. The green dotted histogram represents the DIS contribution to the background.

The electron-energy spectrum falls off sharply above the cut-off value of 10 GeV. The distribution of the electron polar angle falls from the backward region but extends to angular values of about 20°. The distribution of $\ln Q^2$ starts at values of $Q^2$ of about 2 GeV$^2$, peaks at around 150 GeV$^2$, and falls off, eventually reaching zero at $Q^2$ values of around 20000 GeV$^2$. The distribution of $y$ extends between 0 and 1 and peaks at values of about 0.5.

## 5.7 Final Selection

Having demonstrated an understanding of the SM processes which make up the event sample, it is possible to make the final top-specific selections. These selections are based on variables that discriminate between standard high-$p_T$ jet production provided by PYTHIA, RAPGAP and EPVEC packages and single-top events generated by ANOTOP as discussed in Chapter 4.

There are two different samples selected for study. In the first sample, only jet-derived quantities are used. In the second sample the presence of a muon in one of the jets is used to further reduce the background. This makes use of the fact that approximately twenty percent of all heavy-quark decays contain a muon of momentum above $\sim 2$ GeV in one of the jets. In the instance of top-quark decay, these muons come from the decays of the bottom-quark and also from the $W$-boson decay products. This contrasts with a muon fraction of approximately 3% expected in Standard Model high-$p_T$ jet events.

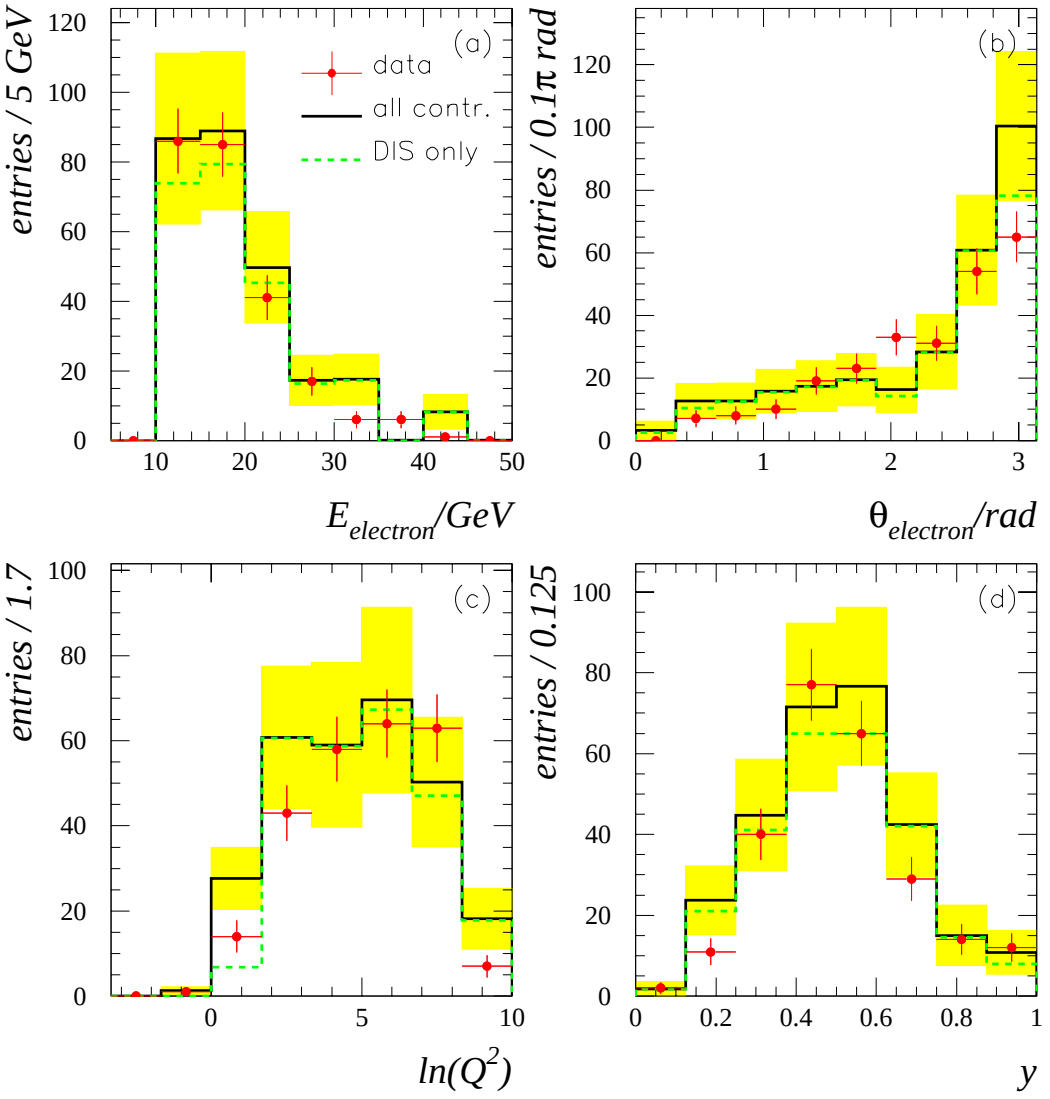


Figure 5.6: Distributions of $E_{electron}$, $\theta_{electron}$, $\ln Q^2$ and $y_{electron}$ as defined in the text. In each diagram, the red points represent the data and the black solid histogram and yellow shaded area represent the simulated background and its error. The green dotted histogram represents the DIS contribution to the background.

### 5.7.1 Discriminating Variables

The variables used in the final single-top selection are defined below.

- The invariant mass of the selected jets $M_{tot}$ is used, as defined and shown previously.

- The invariant mass of the jet pair which falls closest to the $W$ mass. $M_W = min\left(|M_{12} - W_{mass}|, |M_{13} - W_{mass}|, |M_{23} - W_{mass}|\right)$ where $M_{ij}$ is the invariant mass of the two jets $i$ and $j$, and $i$ and $j$ indicate the ordering in $P_T^{jet}$. Here, $W_{mass} = 80.4\,\text{GeV}$.

- The scalar transverse energy of the event. This is defined as the scalar sum of the transverse energies of all the hadrons in the event. Here, $\sum |E_T| = \sum_i |E_{T_i}|$, where the index $i$ runs over all the hadrons in the events.

- $\cos\alpha$. The cosine of the angle between the W jets in the top-quark rest-frame (defined by $p^{\mu}_{jets}$ in the laboratory frame). This is represented pictorially in Figure 5.7.

Hadronic decays of top-quarks are characterised by at least three high-$p_T$ jets (generically one is identified with the bottom-quark and two come from the hadronic decay of the $W$-boson) in the hadronic final-state combined with a large transverse energy, $\sum E_T$, due to the high mass of the top-quark. The invariant mass of all the jets in the event, $M_{tot}$, should be at or around the top-quark mass and at least one pair of jets should have an invariant mass close to the mass of the $W$-boson, $M_W$. This jet pair is then considered as

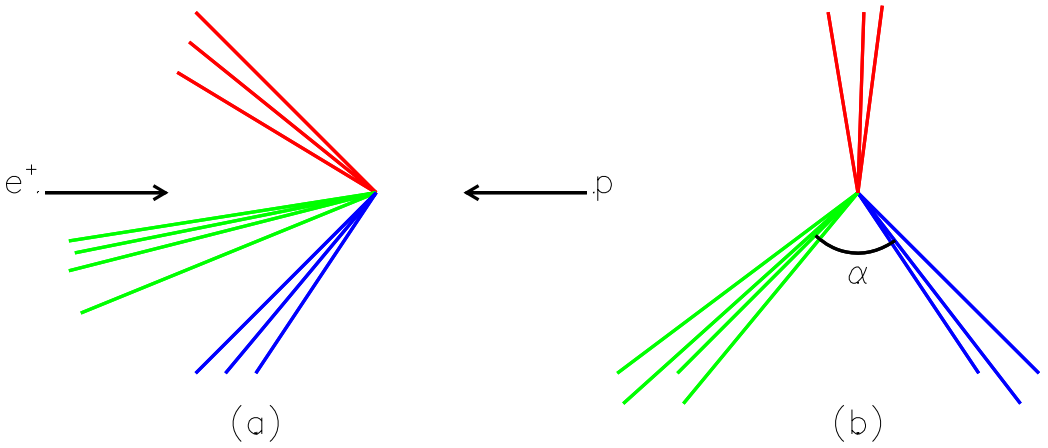


Figure 5.7: (a) shows a schematic representation of a 3-jet event in the laboratory frame. In the analysis the reference frame of the top-quark is defined by vector sum of the jet 4-momenta. The green and blue jets are found to have an invariant mass close to the $W$ mass and are labelled as the $W$-pair. (b) shows a schematic representation of the same jets in the reference frame of the top-quark. The variable $\alpha$ is defined as the angle between the $W$-pair in this frame.

coming from the decay of the $W$-boson. The final discriminating variable, $\cos\alpha$, is the cosine of the angle between these $W$-jets as measured in the rest frame of the top-quark as explained in Figure 5.7.

The comparison of the discriminating variables for the expected background and for the predicted single-top signal are shown in Figure 5.8, where the vertical lines and arrows indicate the regions to be excluded. The single-top simulation histograms have been normalised such that they have an equal area to the simulated background histograms. Figure 5.8(a) shows the distribution of $\sum E_T$. For the simulated background this is an exponentially falling distribution. For the single-top simulation, however, the $\sum E_T$ peaks at around 150 GeV because the high mass of the top-quark creates a large amount of visible energy when it decays. Figure 5.8(b) shows $M_{tot}$, the total

invariant mass of all the jets in the event that pass the $\eta_{jet}$ cut. For the simulated background the spectrum of invariant mass falls monotonically. For the single-top simulation, the distribution peaks at the mass of the top-quark as would be expected. The peak is asymmetric and biased towards lower values because some of the mass of the events is lost when the $\eta$-cuts are applied. This also holds for the distribution of the reconstructed mass of the $W$-boson for the single-top simulation shown in Figure 5.8(c). Although the $M_W$ distribution peaks at 80 GeV, the lower side of the distribution is enhanced when compared with the upper. For the simulated background the distribution falls monotonically. Figure 5.8(d) shows the distribution of $\cos\alpha$. For single-top events in the top-quark rest-frame, the $W$-boson will have a significant momentum, such that when it decays the quark-pair formed will tend to be produced at a narrower closing angle than in the simulated background events, where there is no initial massive particle and a back-to-back jet configuration is the most likely to produce the high mass needed. This has the effect of forcing the single-top events to higher values of $\cos\alpha$.

In Figure 5.9 the comparisons between data events and the simulated backgrounds are shown for these discriminating variables.

### 5.7.2 Muon Selection

Due to their penetrating nature muons are detected in a number of detector components from the innermost to the outermost. Muons show up in the trackers as charged tracks, in the calorimeters as minimally ionizing particles, and are finally detected in the instrumented iron muon systems. Muons

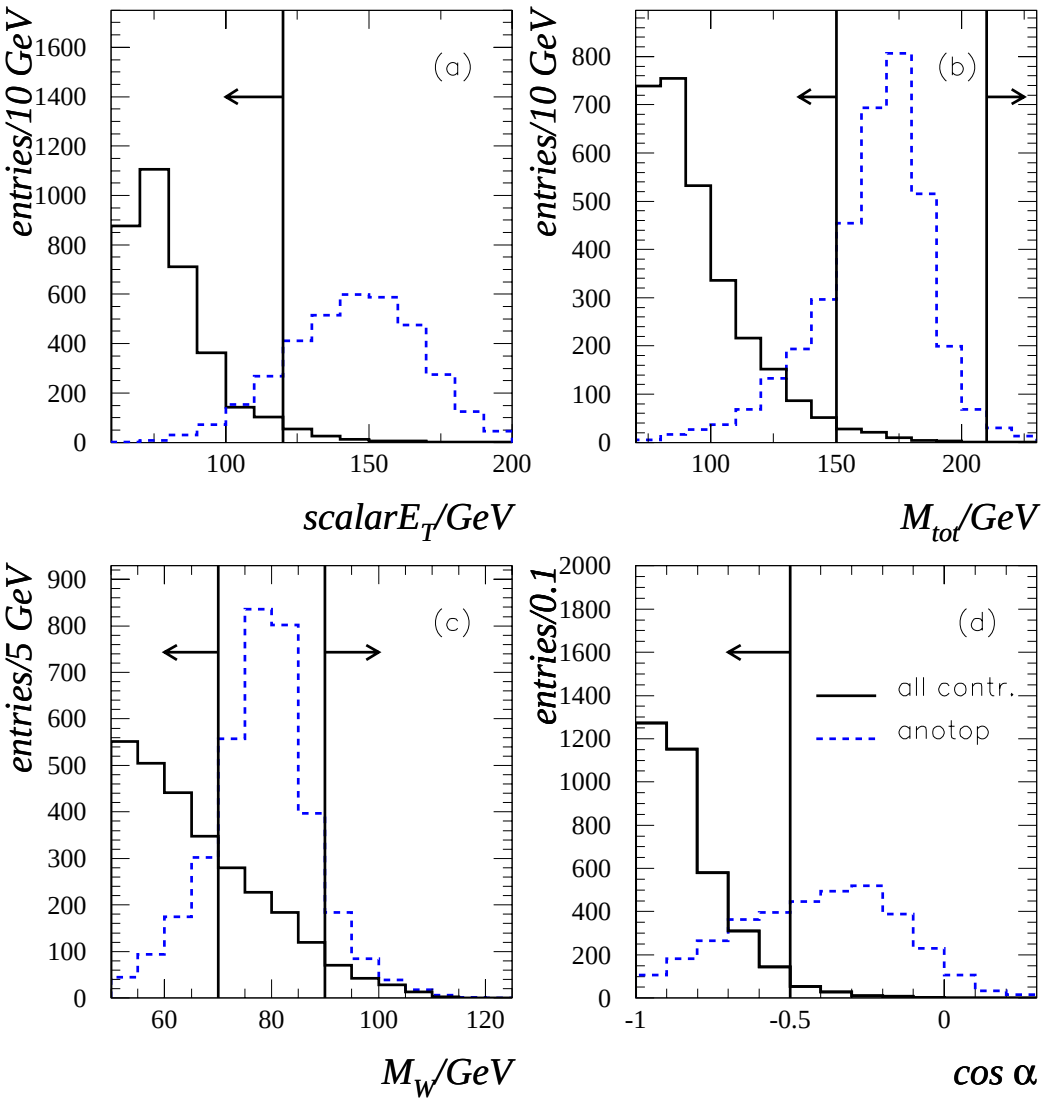


Figure 5.8: Distributions of scalar $\sum E_T$, $M_{tot}$, $M_W$ and $\cos\alpha$. In each case the black solid histogram represents the standard model expectation and the dashed blue histogram represents the prediction for single-top production. The vertical lines illustrate the cuts made on each variable and the arrows indicate the region excluded by the cut.

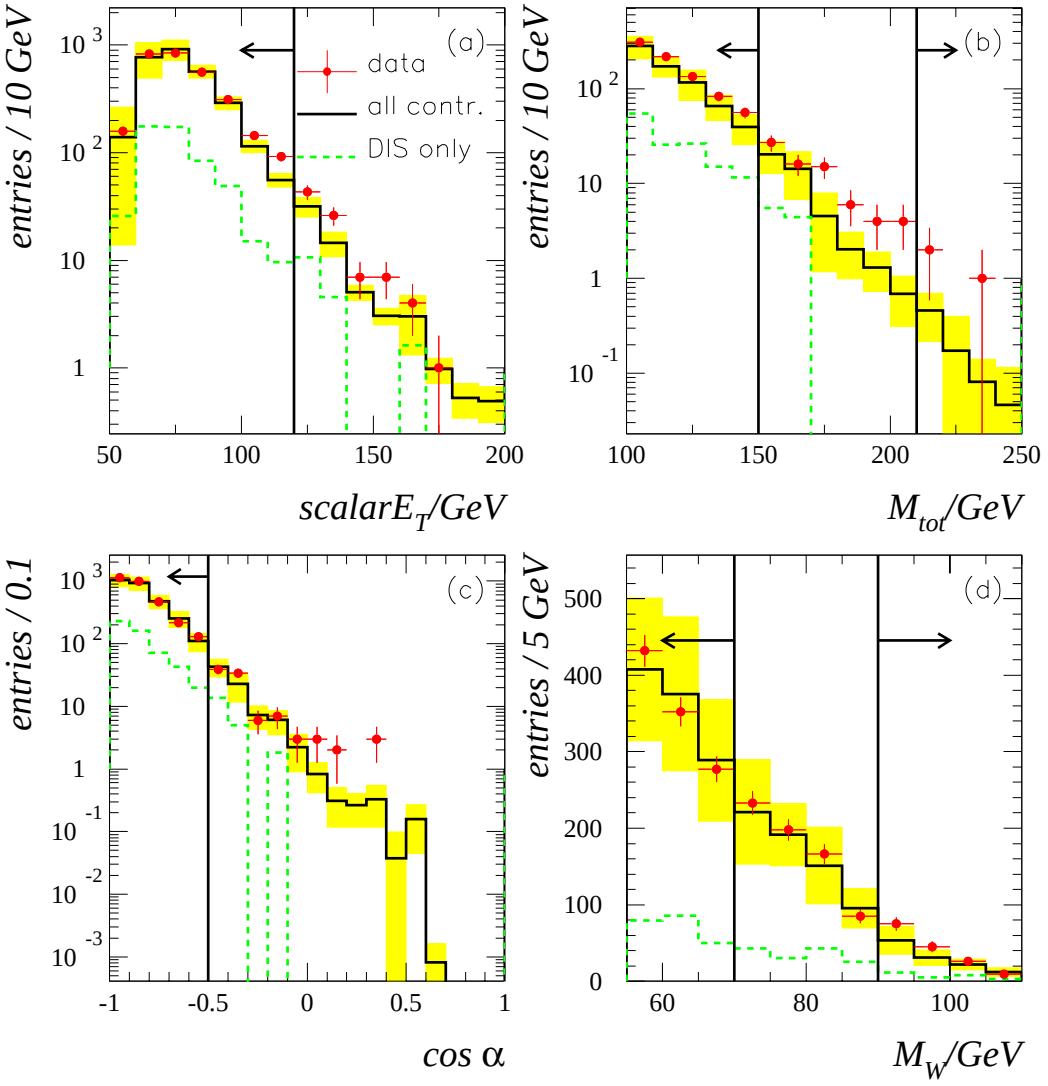


Figure 5.9: Distributions of $\sum E_T$, $M_{tot}$, $\cos\alpha$ and $M_W$ defined in the text. In each diagram, the red points represent the data and the black solid histogram represents the combined contributions to the expected background from the various QCD based models. The yellow shaded area represents the error on the expectation. The green dotted histogram represents the DIS contribution to the background as modelled by RAPGAP. The vertical lines and arrows indicate the area to be excluded.

travelling forward at $\theta \leq 18^{\circ}$ additionally pass through the forward muon systems.

Because the muons analysed here are associated with jets, it is not possible to select muons using only calorimeter information, because the muon signal could be masked by energy deposits left by other particles comprising the jet. Therefore only central muons detected in the instrumented iron detectors are used. Muons tagged using only calorimetric information are rejected. Forward muons are selected only if they show hits in the forward muon detectors. A cut on the transverse-momentum of the muon, $p_T > 2\,\mathrm{GeV}$, is applied to those muons remaining.

The muons are not included in the initial jet-finding algorithm and since they can carry a substantial proportion of the transverse-momentum of the jet they must be included in the invariant mass calculations. The muons are added into the jet to which they are closest in $(\eta - \phi)$ space by simple four-momentum addition. The distributions of the transverse-momentum of the muon $p_T^{\mu}$, the polar angle of the muons track $\theta^{\mu}$, the invariant mass of the events that contain muons including the muon $M_{tot}$, and the scalar transverse energy of the event $\sum E_T$ also including the muon, are shown in Figures 5.10(a), (b), (c) and (d) respectively. As would be expected, the $p_T^{\mu}$ spectrum falls rapidly with rising transverse-momentum and the muon production peaks at low polar angle. The corrected invariant mass and corrected scalar transverse energy are still well described in this new sample.

The comparison of the discriminating variables for the expected background and for the predicted single-top signal are shown in Figure 5.11, where the

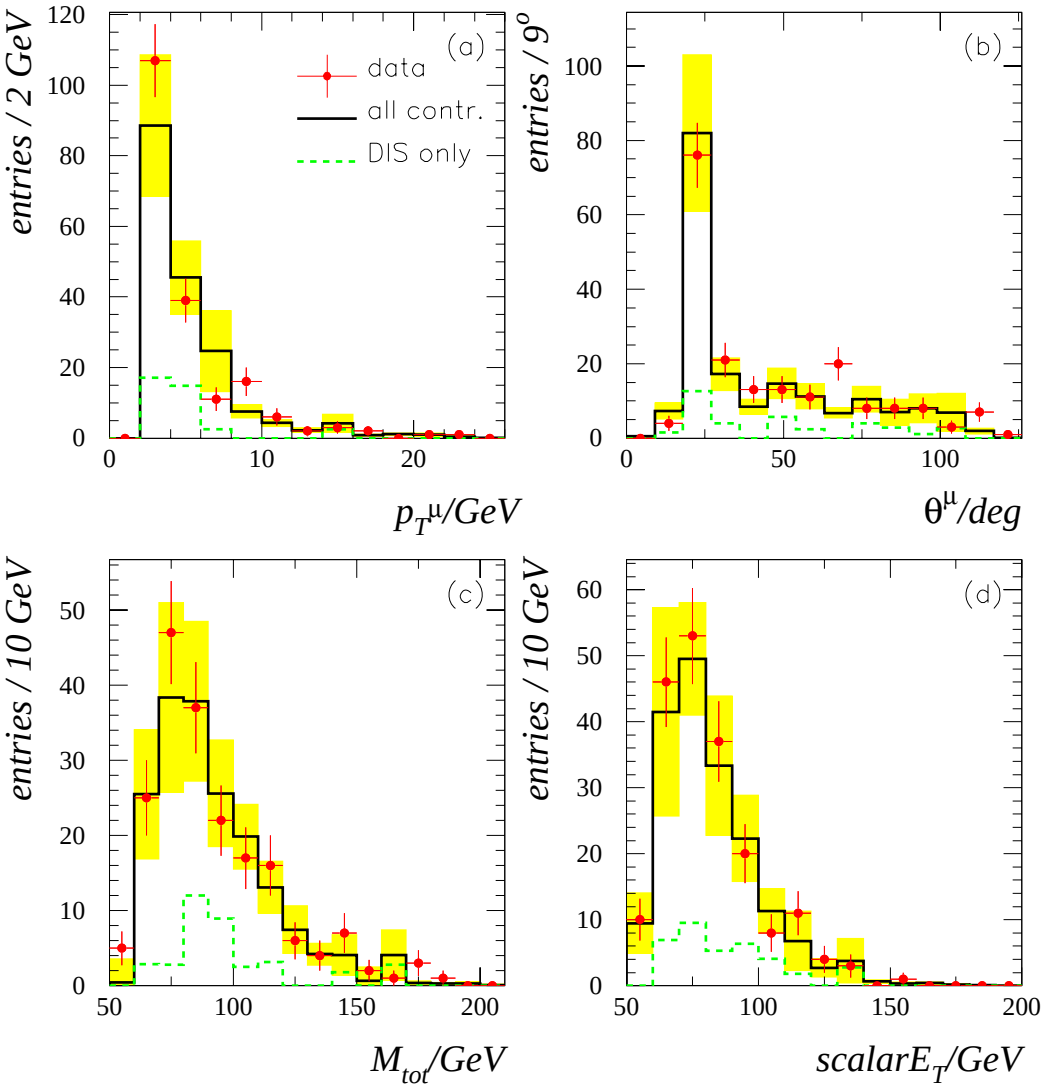


Figure 5.10: Distributions of (a) $p_T^{\mu}$, (b) $\theta^{\mu}$, (c) $M_{tot}$ and (d) $\sum E_T$ as defined in the text for the muon-tagged sample. In each diagram, the red points represent the data and the black solid histograms and yellow shaded area represent the simulated background and its error. The green dotted histogram represents the DIS contribution to the background.

| Cut | Top Eff. (Cum.) | Bground Exp. (Cum.) |
|---|---|---|
| high $p_T$ 3-jet selection | 55% (55%) | 4269 (4269) |
| $scalar E_T > 120$ GeV | 51% (51%) | 85.4 (85.4) |
| 150 GeV$< M_{tot} <$ 210 GeV | 45% (43%) | 59.2 (39.8) |
| 70 GeV$< M_W <$ 90 GeV | 41% (32%) | 958 (28.9) |
| $\cos\alpha > -0.5$ | 37% (26%) | 115 (14.1) |

Table 5.1: List of cuts showing the cut value, percentage of single-top events surviving each cut individually, background expectation after each cut individually, top efficiency after each cut cumulatively, and the background expectation after each cut cumulatively.

vertical lines and arrows indicate the regions to be excluded. The single-top histograms have been normalised such that they have equal areas to the simulated background histograms. Figure 5.11(a), (b), (c) and (d) show the distributions of $\sum E_T$, $M_{tot}$, $M_W$ and $\cos\alpha$ respectively. The form and discussion of these plots is the same as in Section 5.7.1 above, except it should be noted that the relative shapes of the distributions have not been altered significantly by the correction process.

In Figure 5.12 the comparisons between data events and the simulated backgrounds are shown for these discriminating variables.

### 5.7.3 Final Top Selection

The final top-specific cuts applied both to the purely hadronic selection and to the muon-tagged selection are the same. These cuts are listed in Tables 5.1 and 5.2. The resulting event-samples constitute the final single-top selections for the hadronic channel and the muon-tagged channel.

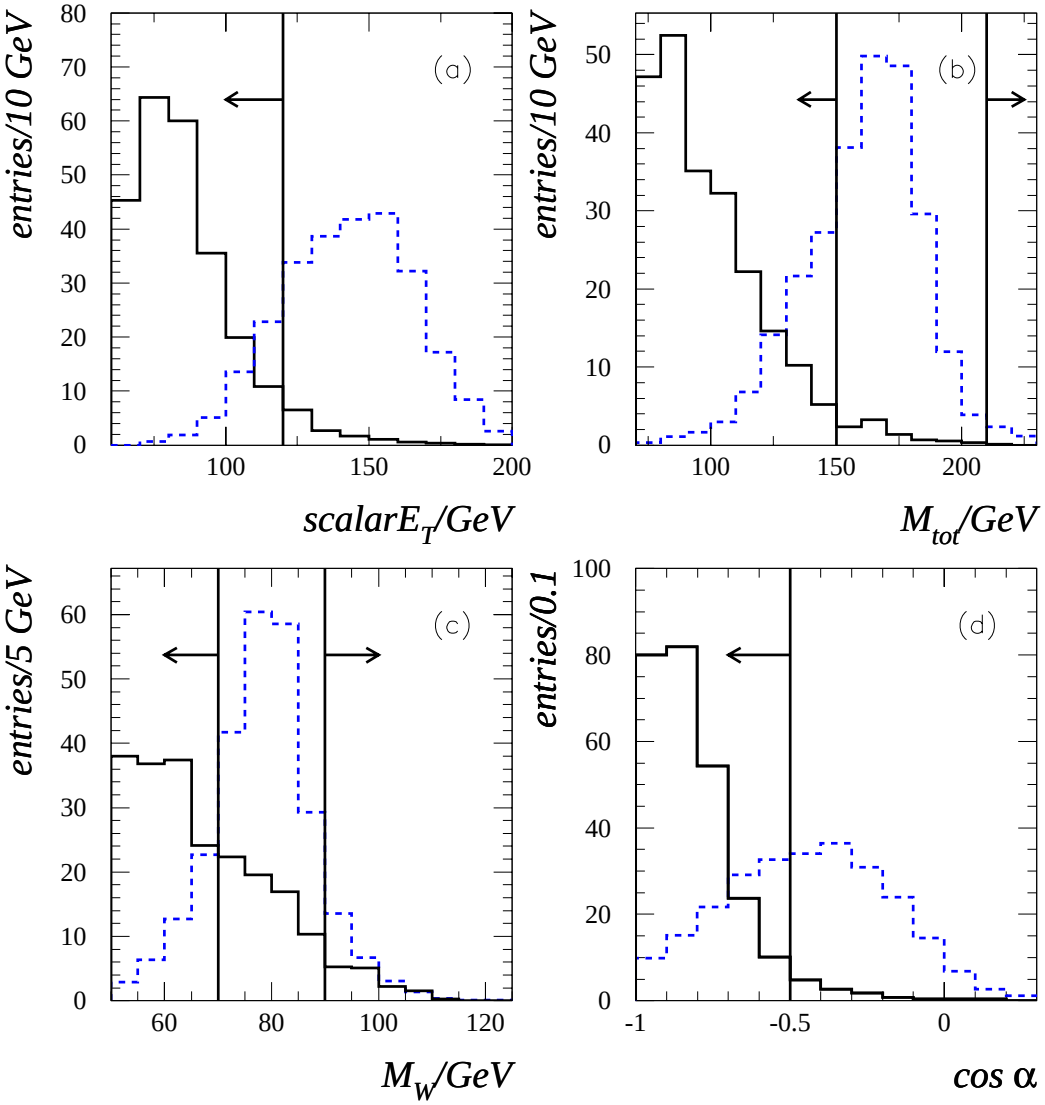


Figure 5.11: Distributions of $\sum E_T$, $M_{tot}$, $M_W$ and $\cos\alpha$ as defined in the text for the muon-tagged sample. In each case, the solid black histogram represents the standard model expectation and the dashed blue histogram represents the prediction for single-top production. The vertical lines illustrate the cuts made on each variable and the arrows indicate the region excluded by each cut.

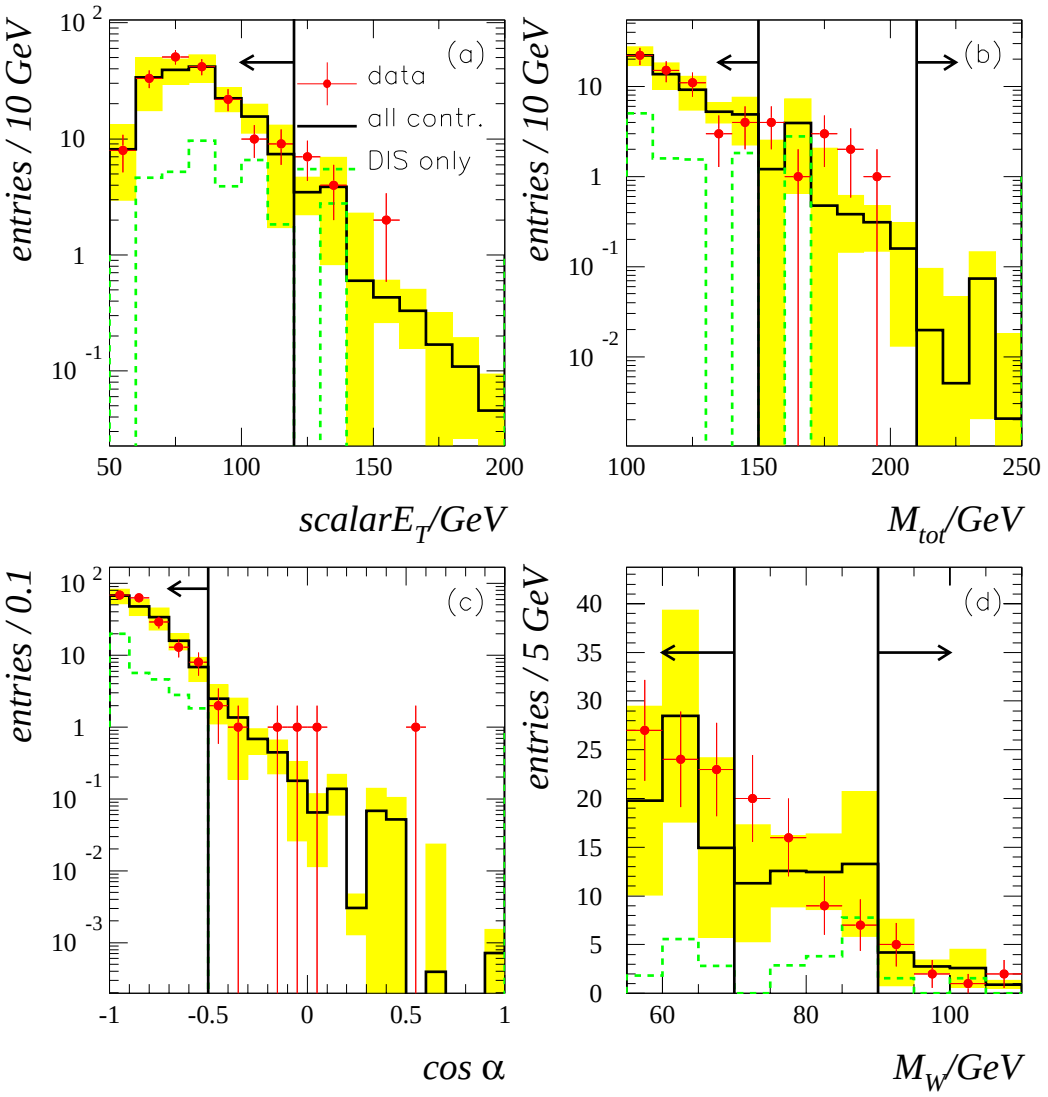


Figure 5.12: Distributions of $\sum E_T$, $M_{tot}$, $\cos\alpha$ and $M_W$ defined in the text for the muon-tagged sample. In each diagram, the red points represent the data and the black solid histogram represents the combined contributions to the expected background from the various QCD based models. The yellow shaded area represents the error on the expectation. The green dotted histogram represents the DIS contribution to the background as modelled by RAPGAP. The vertical lines and arrows indicate the area to be excluded.

| Cut | Top Eff. (Cum.) | Bground Exp. (Cum.) |
|---|---|---|
| high $p_T$ 3-jet $+\mu$ selection | 15% (15%) | 177.3 (177.3) |
| $scalar E_T > 120$ GeV | 14% (14%) | 5.2 (5.2) |
| 150 GeV$< M_{tot} <$ 210 GeV | 12% (12%) | 2.5 (1.7) |
| 70 GeV$< M_W <$ 90 GeV | 11% (8%) | 35.8 (1.2) |
| $\cos\alpha > -0.5$ | 10% (6%) | 3.5. (0.8) |

Table 5.2: List of cuts showing the cut value, percentage of single-top events surviving each cut individually, background expectation after each cut individually, top efficiency after each cut cumulatively, and the background expectation after each cut cumulatively for the muon-tagged channel.

# Chapter 6

# Systematic Errors

As well as the statistical errors present in this analysis that are assumed to follow Poisson statistics a number of sources of systematic error have been considered.

## 6.1 Hadronic Energy Scale

The absolute hadronic energy scale is known to a precision of 4%. The energies of HFS objects were varied by this amount, leading to a significant systematic effect. In the purely hadronic channel the expected variation was found to be $\pm 3.8$ events.

The variation in hadronic energy scale also has an effect on the efficiency for single-top events. With the cuts as stated above, the efficiency has a value of 26% that varies by $\pm 3\%$ when the energies of the hadronic final-state objects are allowed to vary by $\pm 4\%$

## 6.2 QCD Model Uncertainty

The scaling of the QCD-based calculations in order to match data is described in Section 5.5. To determine precisely the uncertainty on the QCD-based models from first principles is not possible. For example, there is no option in PYTHIA for varying the renormalization scale and, more importantly, there is no 'correct' prescription for the variation.

The uncertainty owing to the QCD-based models in this analysis is taken as being half the scaling factor used (10%), which is the variation needed to produce a poor description of data distributions presented in this thesis. This leads to an expected variation of $\pm 1.4$ and $\pm 0.7$ events in the purely hadronic and muon-tagged channels, respectively.

As a further check, the HERWIG model was used to estimate the photo-production contribution. This was found to vary by 33% compared to the PYTHIA prediction, but HERWIG gives a significantly poorer description of the data distributions [96]. Thus, the difference in models was not included as a systematic error.

## 6.3 Uncertainty of Top-Quark Mass

The mass of the top-quark has been measured to be $174.3 \pm 5.1\,\text{GeV}$ [62]. The uncertainty expressed as a percentage is $\sim 3\%$. By varying the energies of objects in the modelled single-top events by 3% the reconstructed mass of the top-quark varies by $\sim 3\%$. This has an effect on the expected efficiency for single-top events. The variation is $\pm 1.5\%$ on the expected efficiency.

## 6.4 Luminosity

A luminosity uncertainty of 1.5% is used, corresponding to the precision of the luminosity measurement [14].

# Chapter 7

# Results of the Single-Top Search

After the selections described in the Chapter 5 are made, a certain sample of the data remains. The selection is also applied to the simulated sample generated from the QCD based models described in Chapter 4. This gives a prediction for the expected background in each channel. The observed and expected event rates are summarised in the Table below

| Selected Sample | Observed | Expected $\pm stat. \pm syst.$ |
|---|---|---|
| Purely Hadronic Sample | 13 | $14.1 \pm 2.7 \pm 4.0$ |
| Muon-Tagged Sample | 2 | $0.8 \pm 0.4 \pm 0.7$ |

No significant excess above the Standard Model expectation is seen in either channel. The selection efficiency for finding single-top events is $26 \pm 4\%$ and $6 \pm 1\%$ in the purely hadronic and muon-tagged channels, respectively. These results can be used to derive an upper limit on the cross section for single-top production as detailed in Appendix A.

## 7.1 Upper Limit on the Single-Top Cross-section

The results summarised in the Table above indicate that no deviation from the Standard Model expectation has been observed. Using the prescription detailed in Appendix A, it is possible to use these results to set a limit on the cross section for single-top production in $ep$ collisions at a centre of mass energy of 320 GeV.

First the separate running periods are combined. The expectations in the purely hadronic channel for each running period are summed and the errors combined in quadrature. The predicted top efficiency is weighted by the luminosities and the ratio of predicted cross sections for each running period according to:

$$\text{top efficiency} = \sum_i \frac{\mathcal{L}_i}{\mathcal{L}_{total}} \frac{\sigma(ep \to etX)_i}{\sigma(ep \to etX)_{\sqrt{s}=320\,\text{GeV}}} \epsilon_i \tag{7.1}$$

where the index $i$ runs over the running periods considered in this analysis, $\mathcal{L}_i$ represents the integrated luminosity collected in that period, $\sigma(ep \to etX)_i$ is the predicted cross-section for single-top production in that period and $\epsilon_i$ is the predicted top efficiency in that period. The same procedure is used to combine the results in the muon-tagged channel.

The total integrated luminosity considered in this analysis is $104.1\,\text{pb}^{-1}$. $35.6\,\text{pb}^{-1}$ of this integrated luminosity was collected at a centre of mass energy of 300 GeV and the remaining $68.5\,\text{pb}^{-1}$ of integrated luminosity was collected at a centre of mass energy of 320 GeV. The predicted cross section for single-top production at 320 GeV is 1.41 times the cross section at

300 GeV.

Thus, combining the results for the purely hadronic single-top sample gives 13 events observed for a Standard Model expectation of $14.1 \pm 4.8$ events. The combined top efficiency is 23.3%. This leads to a derived upper limit on the single-top cross-section at 320 GeV of 0.68 pb at the 95% confidence level.

In the sample where one jet is tagged with a muon, the same procedure gives two events observed for a Standard Model expectation of $0.8 \pm 0.8$ events. The corrected top efficiency is 5.3%. This leads to a derived upper limit on the single-top cross-section at 320 GeV of 1.35 pb at the 95% confidence level. The looser limit derived in this channel comes from its low efficiency compared to the other channel and also to the slight excess in data over expectation.

## 7.2 Isolated Lepton Events

The derived limit on the cross-section can be used to check the hypothesis that the excess of events described in the Introduction, which are characterised by a high-$p_T$ lepton combined with a large missing transverse-momentum and a high transverse-momentum hadronic system, come from the production and semi-leptonic decay of single top-quarks. In $101.6\,\mathrm{pb}^{-1}$ of data an upper limit on the cross-section $\sigma(ep \to etX)$ for single-top pro-

duction would lead to

$$\mathcal{L}\sigma(ep \to etX)\Gamma(t \to Wb)\Gamma(W \to l\overline{\nu_l})\epsilon$$

events in the high $p_T$ lepton channel. Taking $\sigma$ as 0.68 pb, $\Gamma(t \to Wb)$ as 100%, $\Gamma(W \to l\overline{\nu_l})$ as 22% and $\epsilon$, the top efficiency, as 45% [74] leads to an upper limit in the semi-leptonic channel of $\sim 7$ events. Comparing this to the observation of 10 events with an expectation of $2.82 \pm 0.73$ events, we see that the derived upper limit from the hadronic channel cannot rule out the hypothesis that the isolated lepton events seen are caused by single-top production at the 95% confidence level.

## 7.3 Extraction of the Anomalous Coupling

The upper limit on the cross section can also be used to derive a limit on the anomalous coupling $\kappa_{\gamma,u}$. In the scenario outlined in Section 2.5.1 the cross section for single-top production depends only on the square of the anomalous coupling. Extrapolating from the calculated value of 0.21 pb for the cross section at $\kappa_{\gamma u} = 0.15$ to the derived upper limit on the cross section of 0.68 pb leads to an upper limit on the coupling of

$$\kappa_{\gamma,u} < 0.27 \,\text{at}\, 95\% \,\text{C.L.}.$$

The cross section derived in the muon-tagged channel gives an upper limit

on the coupling of

$$\kappa_{\gamma,u} < 0.38 \,\text{at}\, 95\% \,\text{C.L.}.$$

Both these limits are better than previous published limits from the CDF collaboration [69]. Limits from preliminary LEP analyses have improved on the CDF limit. The LEP limit of $\kappa_{\gamma u} < 0.35$ [101] is slightly better than the limit derived from the muon-tagged channel in this analysis. However, the best upper-limit derived here is more stringent than limits from LEP and CDF.

# Chapter 8

# Conclusion

In a search for the production and subsequent hadronic decay of single top-quarks at H1 using a total of $104\,\mathrm{pb}^{-1}$ of data gathered between 1994 and 2000, no significant excess of events was observed. With a predicted signal efficiency for single-top production of 23.3% and an expected background coming from multi-jet photoproduction and DIS of $14.1 \pm 4.8$ events, 13 events were observed. These figures give an upper limit on the cross section, $\sigma(ep \to etX,\ \sqrt{s} = 320\,\mathrm{GeV})$, of 0.68 pb at the 95% confidence level.

In an additional search, in which at least one of the jets in the event must contain a muon, the predicted single-top efficiency was 5.3% and the expected background was $0.8 \pm 0.8$ events. Two events were observed, leading to an upper limit on the cross-section for single-top production of 1.35 pb at the 95% confidence level. The larger limit in this channel is due chiefly to the low efficiency of the signal in this channel.

The derived limit on the cross-section was also used to test the hypothesis

that the excess of events described in the Introduction, and characterised by a high-$p_T$ lepton combined with large missing transverse-momentum and a high transverse-momentum hadronic system, come from the production and semi-leptonic decay of single top-quarks. The derived upper-limit from the hadronic channel cannot rule out the hypothesis that the isolated lepton events seen are caused by single-top production at the 95% confidence level.

The upper limit on the cross-section was also used to set a limit on the anomalous coupling $\kappa_{\gamma u}$, the FCNC reaction coupling the $u$ quark to the photon and top-quark. The previous best limit comes from the LEP collaboration [101], where searches for the process $e^+e^- \rightarrow ut$ lead to a limit of

$$\kappa_{\gamma u} < 0.35.$$

Using this value leads to a predicted cross section of $\sim 1\,\text{pb}$ for the reaction $\sigma(ep \rightarrow etX, \sqrt{s} = 320\,\text{GeV})$. This is considerably higher than the limit derived in the analysis presented in this thesis, which leads to a new upper bound,

$$\kappa_{\gamma u} < 0.27.$$

Figure 8.1 shows the exclusion limits set by the different experiments in the $\kappa_{\gamma u}, v_{Zu}$ plane. $v_{Zu}$ is the anomalous coupling between the $Z$-boson and the up- and top-quarks. The H1 limit on $\kappa_{\gamma u}$ is compared to the limits from CDF [69] and LEP2 [101]. The CDF limits on the $\gamma$ and $Z$ couplings come from direct searches for the decays $t \rightarrow q\gamma$ and $t \rightarrow qZ$, and so each coupling is excluded separately. The LEP2 exclusion boundary is curved due to the

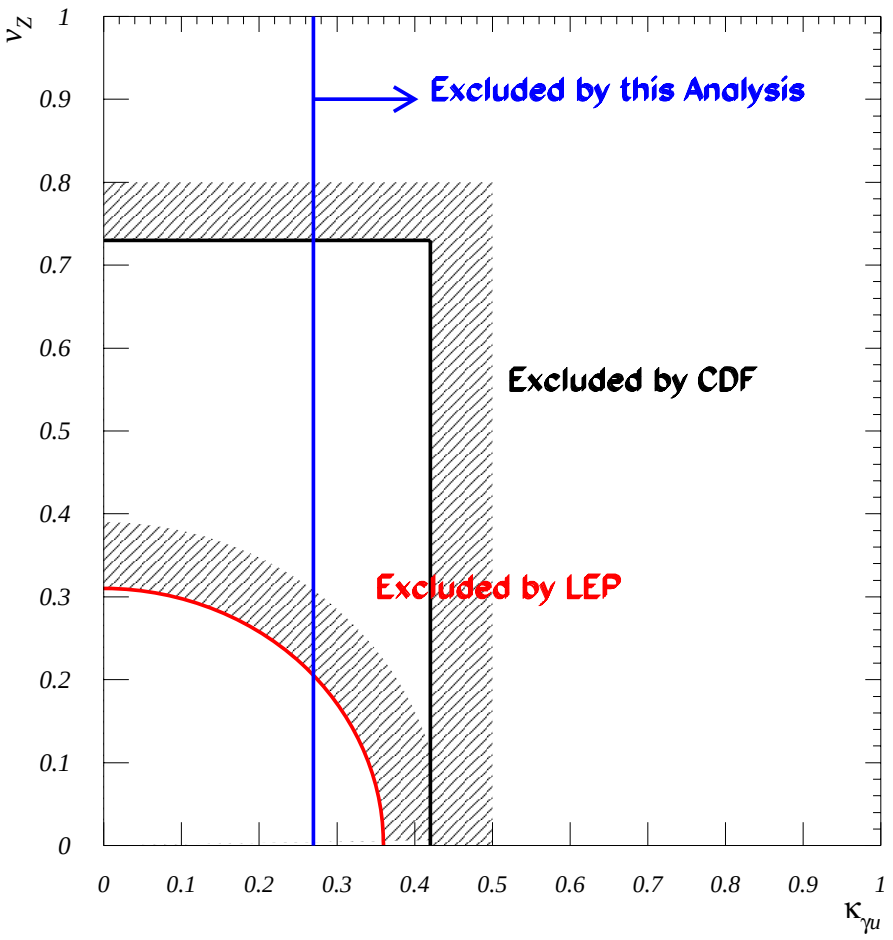


Figure 8.1: Exclusion limits at the 95% Confidence Level on the anomalous $tq\gamma$ magnetic coupling $\kappa_\gamma$ and the vector coupling $v_Z$ obtained at the TEVATRON, LEP and HERA colliders. The HERA limit applies to the coupling $\kappa_{\gamma u}$ to the $u$-quark only.

mixing of the $Z$ boson and the photon. The LEP limit comes from a search for the process $e^+e^- \rightarrow qt$ and is sensitive to couplings both to the $Z$ boson and the photon.

## 8.1 Future Prospects

HERA was shut down in 2000 in order for upgrades to be made to the HERA machine and the experiments that rely on it. When HERA restarts it will do so with the aim of providing a far higher luminosity than previously, and by the end of its run in 2005 it is hoped that $1\,\mathrm{fb}^{-1}$ of data will have been collected. The question is, "how will this affect the search for single-top physics and flavour-changing neutral-current interactions?"

In the first instance it will be interesting to see the rate at which the isolated lepton events occur after the upgrade. Currently the hypothesis that the events are due to single-top production cannot be ruled out. However, if it is assumed that the isolated lepton events continue to occur at the pre-shutdown rate and that no excess appears in the hadronic top channel then the single-top hypothesis for the isolated lepton events could be ruled out with a factor-two increase in luminosity, i.e. $\sim 200\,\mathrm{pb}^{-1}$. At this luminosity $\kappa_{\gamma u}$ would be constrained to be lower than 0.22 at the 95% Confidence Level.

For an integrated luminosity of $1\,\mathrm{fb}^{-1}$ at HERA, and again assuming that no excess is seen in the hadronic channel, the cross section limit for single-top production would be $\sim 0.15\,\mathrm{pb}$, giving an upper limit of $\kappa_{\gamma u} = 0.14$ at the 95% Confidence Level. However, Run II of the TEVATRON is expected to

exclude down to values of $\kappa_{\gamma u} < 0.06$ with $10\,\text{fb}^{-1}$ of integrated luminosity and the LHC is expected to exclude down to $\kappa_{\gamma u} < 0.005$ with $100\,\text{fb}^{-1}$ [68].

# Appendix A

# Derivation of Limits

Two possible contributions to the observed event-yield in any channel are considered. One contribution comes from the expected Standard Model background, which is known to some degree from event generators and theoretical predictions. The second contribution is a possible contribution from single-top production, which also has an associated efficiency. It is supposed that each of these components obeys Poisson statistics. The Poisson parameter for the background process, $\mu_B$, can be estimated from Monte Carlo event generators. The number of background events surviving all cuts is taken as the estimate for $\mu_B$. The Poisson parameter for the expected signal is denoted as $a$. The probability of observing $n$ events is given by

$$P = \frac{1}{n!} e^{-(a+\mu_B)} (a + \mu_B)^n \tag{A.1}$$

Now consider the inverse problem. If $n_0$ events have been observed, the probability density for the Poisson parameter, $a$, of the signal is then given

via Bayes' theorem[1] by

$$g(a) = N_1 \frac{1}{n_0!} e^{-(a+\mu_B)} (a + \mu_B)^{n_0} \tag{A.2}$$

where $N_1$ is the normalisation constant such that:

$$\int_0^\infty g(a)da = 1 \tag{A.3}$$

Consider $A$, the value of $a$ that gives the desired confidence level, $CL$, defined by

$$CL(A) = \int_0^A g(a)da \tag{A.4}$$

Now consider $h(a)$ such that $g(a) = N_1 h(a)$. $N_1$ is then given by

$$N_1 = \frac{1}{\int_0^\infty h(a)da} \tag{A.5}$$

The confidence level is then given by

$$CL = \frac{\int_0^A h(a)da}{\int_0^\infty h(a)da} \tag{A.6}$$

Integrating $h$ by parts gives

$$CL = 1 - \frac{e^{-(\mu_B+A)} \sum_{n=0}^{n_0} \frac{1}{n!} (\mu_B + A)^n}{e^{-\mu_B} \sum_{n=0}^{n_0} \frac{1}{n!} \mu_B^n} \tag{A.7}$$

[1]Bayes' theorem can be stated as $P(A_1 \mid B) = \frac{P(A_1)P(B|A_1)}{\sum_i P(A_i)P(B|A_i)}$ where $P(x)$ is the probability of an event $x$ occurring and $P(x \mid y)$ is the probability that event $x$ occurs given that event $y$ has occurred.

The summations in the previous equation can be written as integrals using a function $\chi^2$ of $2(n_0+1)$ degrees of freedom.

$$e^{-n}\sum_{k=0}^{k=N}\frac{n^k}{k!}=\int_{2N}^{\infty}\chi^2(2(n+1)) \tag{A.8}$$

The Confidence Limit can now be written as

$$\int_{2(N_{bground}+A)}^{\infty}\chi^2(2(n_0+1))=(1-CL)\int_{2N_{bground}}^{\infty}\chi^2(2(n_0+1)) \tag{A.9}$$

This rewriting of the equation in terms of the function $\chi^2$ is not entirely without reason. This manipulation allows the use of computer functions that reverse the integrals of the $\chi^2$ function. For example, using CERNLIB [102] library routines, $A$ is given by,

$$A=\frac{1}{2}\left\{CHISIN\left[1-(1-CL)PROB(2N_{bground},ndf),ndf\right]\right\}-N_{bground} \tag{A.10}$$

where $ndf=2(n_0+1)$. After finding $A$ in this way the cross-section limit for the chosen Confidence Level can be deduced via

$$A=L\epsilon\sigma$$

where $\epsilon$ is the predicted efficiency of the signal after all the selection cuts are applied.

## A.1 Including Systematic Uncertainties

In practice, the knowledge of both the background and signal processes is limited by systematic and statistical uncertainties. The derivation of the upper limit in the previous section does not take these into account, but they can be accounted for in a similar framework. By allowing $\mu_B$ to vary with its own probability density function, $f(\mu_B)$, equation A.1 can be rewritten as:

$$P = \int_0^\infty \frac{1}{n!} e^{-(\mu'_B+N)} (\mu'_B + N)^n f(\mu'_B) d\mu'_B. \tag{A.11}$$

Setting $f(\mu'_B) = \delta(\mu'_B - \mu_B)$ here recovers the original Poisson distribution shown in equation A.1. The uncertainty on the signal efficiency can be treated in a similar way by convoluting $P$ again with a function $f(N')$. For clarity, only the treatment of the background errors is included below. In the instance considered here, $f(\mu'_B)$ is assumed to take a Gaussian form and $\mu_B$ is quoted with some error as $\mu_B \pm \sigma_{\mu_B}$. The form of $P$ is now

$$P = \int_0^\infty \frac{1}{n!} e^{-(\mu'_B+N)} (\mu'_B + N)^n \frac{1}{\sqrt{2\pi\sigma^2_{\mu_B}}} e^{-\frac{(\mu'_B-\mu_B)^2}{2\sigma^2_{\mu_B}}} d\mu'_B \tag{A.12}$$

Following the analysis as above this new function for $P$ gives the confidence level $CL$ as

$$CL = \frac{\int_{\mu'_B=0}^\infty \int_{a'=0}^A \frac{1}{n_0!} e^{-(\mu'_B+a')} (\mu'_B + a')^{n_0} e^{-\frac{(\mu'_B-\mu_B)^2}{2\sigma^2_{\mu_B}}} d\mu'_B da'}{\int_{\mu'_{B=0}}^\infty \int_{a'=0}^\infty \frac{1}{n_0!} e^{-(\mu'_B-a')} (\mu'_B + a')^{n_0} e^{-\frac{(\mu'_B-\mu_B)^2}{2\sigma^2_{\mu_B}}} d\mu'_B da'} \tag{A.13}$$

which is then solved numerically for $A$.

# Bibliography


[1] F. Abe et al., Phys. Rev. Lett. **74**, 2626 (1995).

[2] S. Abachi et al., Phys. Rev. Lett. **74**, 2632 (1995).

[3] K. Hagiwara et al., Phys. Rev. **D66**, 010001 (2002).

[4] U. Baur and J. J. van der Bij, Nucl. Phys. **B304**, 451 (1988).

[5] D. Atwood, L. Reina, and A. Soni, Phys. Rev. **D53**, 1199 (1996).

[6] G. M. de Divitiis, R. Petronzio, and L. Silvestrini, Nucl. Phys. **B504**, 45 (1997).

[7] R. D. Peccei and X. Zhang, Nucl. Phys. **B337**, 269 (1990).

[8] H. Fritzsch, Phys. Lett. **B224**, 423 (1989).

[9] T. Ahmed et al., DESY-94-248.

[10] C. Diaconu et al., Talk presented at DIS 2001, April 2001 (2001), C. Diaconu, talk presented at DIS 2001, April 2001.

[11] I. Abt et al., Nucl. Instrum. Meth. **A386**, 348 (1997).

[12] I. Abt et al., Nucl. Instrum. Meth. **A386**, 310 (1997).

[13] J. McGreevy, L. Susskind, and N. Toumbas, JHEP **06**, 008 (2000).

[14] S. Levonian et al., http://www-h1.desy.de/h1/www/h1det/lumi/ (2000).

[15] S. Burke et al., Nucl. Instrum. Meth. **A373**, 227 (1996).

[16] J. Burger et al., Nucl. Instrum. Meth. **A279**, 217 (1989).

[17] S. Prell, Hamburg DESY - Internal Rep. FH1T-92-04 (92/10,rec.Nov.) 92 p.

[18] S. Egli et al., Nucl. Instrum. Meth. **A283**, 487 (1989).

[19] J. Haack, *Calibration of the outer Z drift chamber of the HERA H1 experiment*, PhD thesis, Humboldt University, 1994.

[20] W. Eick et al., Nucl. Instrum. Meth. **A386**, 81 (1997).

[21] M. Biddulph, *Scale dependence of the charm production cross section in photoproduction and performance of the central silicon tracker at the H1 experiment*, PhD thesis, Siegen University, 1997, ETH-12331.

[22] C. Adloff et al., Nucl. Phys. **B497**, 3 (1997).

[23] K. Muller et al., Nucl. Instrum. Meth. **A312**, 457 (1992).

[24] B. Andrieu et al., Nucl. Instrum. Meth. **A336**, 460 (1993).

[25] B. Andrieu et al., Nucl. Instrum. Meth. **A344**, 492 (1994).

[26] B. Heinemann, *Measurement of charged current and neutral current cross sections in positron proton collisions at s**(1/2) approx. 300-GeV*, PhD thesis, Universitat Hamburg, 1999, DESY-THESIS-1999-046.

[27] J. Ban et al., Nucl. Instrum. Meth. **A372**, 399 (1996).

[28] S. Aid et al., Nucl. Phys. **B470**, 3 (1996).

[29] R. D. Appuhn et al., Nucl. Instrum. Meth. **A386**, 397 (1997).

[30] A. Meyer, *Measurement of the structure function F2(x,Q**2) of the proton at low Q**2 with the H1 detector at HERA using the new detector components Spacal and BDC*, PhD thesis, Hamburg University, 1997, DESY-FH1-97-01.

[31] C. Adloff et al., submitted to Phys. Lett. B (2002).

[32] M. Ruffer, *Implementing the silicon instrumented PLUG calorimeter in the H1 detector*, PhD thesis, Hamburg University, 1993, DESY-FH1K-93-01.

[33] P. Biddulph et al., Nucl. Instrum. Meth. **A340**, 304 (1994).

[34] J. Heatherington et al., H1 internal note 93-307 (1993).

[35] J. Heatherington et al., H1 internal note 94-362 (1994).

[36] H. Bethe and W. Heitler, Proc. Roy. Soc. Lond. **A146**, 83 (1934).

[37] P. Renton, Cambridge, UK: Univ. Pr. (1990) 596 p.

[38] I. J. R. Aitchison and A. J. G. Hey, BRISTOL, UK: HILGER (1989) 571p.

[39] e. . Watkins, P. M., Chilton, UK: Rutherford Lab. (2000) 359 p.

[40] D. h. Perkins, Reading, Usa: Addison-wesley ( 1982) 437p.

[41] F. Halzen and A. D. Martin, New York, Usa: Wiley ( 1984) 396p.

[42] J. D. Bjorken and E. A. Paschos, Phys. Rev. **185**, 1975 (1969).

[43] R. P. Feynman, Phys. Rev. Lett. **23**, 1415 (1969).

[44] C. G. Callan and D. J. Gross, Phys. Rev. Lett. **22**, 156 (1969).

[45] J. D. Bjorken, Phys. Rev. **179**, 1547 (1969).

[46] A. C. Benvenuti et al., Phys. Lett. **B223**, 485 (1989).

[47] Z. Zhang et al., talk presented at DIS 2001, April 2001 (2001), Z. Zhang, talk presented at DIS 2001, April 2001.

[48] R. G. Roberts, Cambridge, UK: Univ. Pr. (1990) 182 p. (Cambridge monographs on mathematical physics).

[49] J. Dias de Deus and S. Jadach, Phys. Lett. **B70**, 73 (1977).

[50] G. Altarelli and G. Parisi, Nucl. Phys. **B126**, 298 (1977).

[51] V. N. Gribov and L. N. Lipatov, Yad. Fiz. **15**, 781 (1972).

[52] Y. L. Dokshitzer, Sov. Phys. JETP **46**, 641 (1977).

[53] T. Ahmed et al., Phys. Lett. **B299**, 374 (1993).

[54] J. J. Sakurai, Annals Phys. **11**, 1 (1960).

[55] M. Gell-Mann and F. Zachariasen, Phys. Rev. **124**, 953 (1961).

[56] T. H. Bauer, R. D. Spital, D. R. Yennie, and F. M. Pipkin, Rev. Mod. Phys. **50**, 261 (1978).

[57] A. Levy, J. Phys. **G19**, 1489 (1993).

[58] C. F. von Weizsacker, Z. Phys. **88**, 612 (1934).

[59] E. J. Williams, Phys. Rev. **45**, 729 (1934).

[60] S. Frixione, M. L. Mangano, P. Nason, and G. Ridolfi, Phys. Lett. **B319**, 339 (1993).

[61] S. W. Herb et al., Phys. Rev. Lett. **39**, 252 (1977).

[62] D. E. Groom et al., Eur. Phys. J. **C15**, 1 (2000).

[63] S. Willenbrock, Rev. Mod. Phys. **72**, 1141 (2000).

[64] E. H. Simmons, Boulder 2000, Flavor physics for the millennium* 579-621 (2000).

[65] I. I. Y. Bigi, Y. L. Dokshitzer, V. A. Khoze, J. H. Kuhn, and P. M. Zerwas, Phys. Lett. **B181**, 157 (1986).

[66] M. Kobayashi and T. Maskawa, Prog. Theor. Phys. **49**, 652 (1973).

[67] G. Eilam, J. L. Hewett, and A. Soni, Phys. Rev. **D44**, 1473 (1991).

[68] T. Han and J. L. Hewett, Phys. Rev. **D60**, 074015 (1999).

[69] F. Abe et al., Phys. Rev. Lett. **80**, 2525 (1998).

[70] A. T. Alan and A. Senol, hep-ph/0202119 (2002).

[71] A. Belyaev and N. Kidonakis, Phys. Rev. **D65**, 037501 (2002).

[72] A. D. Martin, R. G. Roberts, W. J. Stirling, and R. S. Thorne, Eur. Phys. J. **C4**, 463 (1998).

[73] J. Breitweg et al., Submitted to the XXXth International Conference on High Energy Physics, Osaka, Japan (2000).

[74] N. Malden et al., Talk presented at DIS 2002 (2002).

[75] T. Sjostrand, hep-ph/9508391 (1995).

[76] G. Corcella et al., JHEP **01**, 010 (2001).

[77] G. Marchesini et al., Comput. Phys. Commun. **67**, 465 (1992).

[78] T. Sjostrand, Comput. Phys. Commun. **82**, 74 (1994).

[79] M. Gluck, E. Reya, and A. Vogt, Phys. Rev. **D46**, 1973 (1992).

[80] H. Jung, Comp. Phys. Commun. **86**, 147 (1995).

[81] A. Kwiatkowski, H. Spiesberger, and H. J. Mohring, Comp. Phys. Commun. **69**, 155 (1992).

[82] U. Baur, J. A. M. Vermaseren, and D. Zeppenfeld, Nucl. Phys. **B375**, 3 (1992).

[83] C. Diaconu et al., unpublished (1999).

[84] E. E. Boos, M. N. Dubinin, V. A. Ilin, A. E. Pukhov, and V. I. Savrin, (1994).

[85] S. Kawabata, Comput. Phys. Commun. **41**, 127 (1986).

[86] R. Brunt et al., CERN-DD/EE 84-1 (1987).

[87] R. Brun, R. Hagelberg, M. Hansroul, and J. C. Lassalle, CERN-DD-78-2-REV.

[88] S. Peters, *Die Parameterisierte Simulation Elektromagnetischer Schauer*, PhD thesis, Universitat Hamburg, 1992.

[89] M. Rudowicz, *Hadronische Schauersimulation fuer den H1-detektor*, PhD thesis, Universitat Hamburg, 1992.

[90] M. H. Seymour, Batavia Collider Workshop 1995:0568-587 (1995).

[91] S. Bethke et al., Phys. Lett. **B213**, 235 (1988).

[92] S. D. Ellis and D. E. Soper, Phys. Rev. **D48**, 3160 (1993).

[93] S. Catani, Y. L. Dokshitzer, M. H. Seymour, and B. R. Webber, Nucl. Phys. **B406**, 187 (1993).

[94] M. H. Seymour, Nucl. Phys. **B513**, 269 (1998).

[95] J. Ebert, J. Marks, A. Mehta, J. Phillips, and L. West, http://www-h1.desy.de/iwork/iescale/hfs/hfs.html (2001).

[96] P. Bate, *High Transverse Momentum 2-jet and 3-jet Cross Section Measurements in Photoproduction*, PhD thesis, University of Manchester, UK, 1999.

[97] S. Frixione and G. Ridolfi, Nucl. Phys. **B507**, 315 (1997).

[98] C. Adloff et al., submitted to Eur. Phys. J. C (2002).

[99] S. Chekanov et al., Eur. Phys. J. **C23**, 615 (2002).

[100] U. Bassler et al., http://www-h1.desy.de/iwork/iescale/qescat/qescat.html (1996).

[101] L. ALEPH, DELPHI, OPAL, and the LEP EXOTICA working group, contributed paper submitted to Summer 2001 Conferences, LEP Exotica WG 2001-01, ALEPH 2001-055 CONF 2001-035, DELPHI 2001-119 CONF542, L3 Note 2706, OPAL TN698 (2001).

[102] Computing and Networks Division, http://wwwinfo.cern.ch/asdoc/psdir/shortwrups.dir/cernlib.ps.gz (1997).